

# Modern Precipitation $\delta^{18}\text{O}$ and Trajectory Analysis over the Himalaya-Tibet Orogen from ECHAM5-wiso Simulations

Jingmin Li<sup>1,2</sup>, Todd A. Ehlers<sup>1\*</sup>, Sebastian Mutz<sup>1</sup>, Christian Steger<sup>2</sup>, Heiko Paeth<sup>2</sup>,  
Martin Werner<sup>3</sup>, Christopher J. Poulsen<sup>4</sup> and Ran Feng<sup>4,5</sup>

1: Department of Geosciences, University of Tuebingen, Germany

2: Institute of Geography and Geology, University of Wuerzburg, Germany

3: Climate Science Division, Alfred Wegener Institute, Germany

4: Department of Earth and Environmental Sciences, University of Michigan, USA

5: National Center for Atmospheric Research, USA

\* Corresponding author: Todd A. Ehlers, [todd.ehlers@uni-tuebingen.de](mailto:todd.ehlers@uni-tuebingen.de),

Wilhelmstrasse 56, 72074 Tuebingen, Germany, University of Tuebingen,

Department of Geosciences.

## Key Points

- (1) Precipitation  $\delta^{18}\text{O}$  over the Tibetan Plateau is simulated with a global climate model.
- (2) Predicted precipitation  $\delta^{18}\text{O}$  over Tibet agrees with the available observations

This is the author manuscript accepted for publication and has undergone full peer review but has not been through the copyediting, typesetting, pagination and proofreading process, which may lead to differences between this version and the Version of Record. Please cite this article as doi: [10.1002/2016JD024818](https://doi.org/10.1002/2016JD024818)

- (3) Analysis of vapor trajectories and extreme daily  $\delta^{18}\text{O}$  values explains spatial and temporal variations in  $\delta^{18}\text{O}$ .

## Abstract

Variations in oxygen isotope ratios ( $\delta^{18}\text{O}$ ) measured from modern precipitation and geologic archives provide a promising tool for understanding modern and past climate dynamics, as well as tracking elevation changes over geologic time. In areas of extreme topography, such as the Tibetan Plateau, the interpretation of  $\delta^{18}\text{O}$  has proven challenging. This study investigates the climate controls on temporal (daily and 6-hr intervals) and spatial variations in present-day precipitation  $\delta^{18}\text{O}$  ( $\delta^{18}\text{O}_p$ ) across the Tibetan Plateau using a 30-year record produced from the ECHAM5-wiso global atmospheric general circulation model (GCM). Results indicate spatial and temporal agreement between model-predicted  $\delta^{18}\text{O}_p$  and observations. Large daily  $\delta^{18}\text{O}_p$  variations of -25 to +5 ‰ occur over the Tibetan Plateau throughout the 30 simulation years, along with interannual  $\delta^{18}\text{O}_p$  variations of ~2‰. Analysis of extreme daily  $\delta^{18}\text{O}_p$  indicates that extreme low values coincide with extreme highs in precipitation amount. During the summer, monsoon vapor transport from the north and southwest of the plateau generally corresponds with high  $\delta^{18}\text{O}_p$  whereas vapor transport from the Indian Ocean corresponds with average to low  $\delta^{18}\text{O}_p$ . Thus, vapor source variations are one important cause of the spatial-temporal differences in  $\delta^{18}\text{O}_p$ .

**Comparison of GCM and Rayleigh Distillation Model (RDM) predicted  $\delta^{18}\text{O}_p$  indicates a modest agreement for the Himalaya region (averaged over 86°-94° E), confirming application of the simpler RDM approach for estimating  $\delta^{18}\text{O}_p$  lapse rates across Himalaya.**

### **Index Terms and Keywords**

**Index Terms:** 1041 - Geochemistry: Stable Isotope Geochemistry, 1854 - Hydrology: Precipitation, 3305 - Atmospheric Processes: Climate Variability, 3337 - Atmospheric Process: Global climate models, 9320 - Geographic Location: Asia.

**Keywords:** Himalaya, Tibet, Precipitation  $\delta^{18}\text{O}$ , ECHAM5-wiso, trajectory analysis, Rayleigh distillation.

### **1. Introduction**

Long-term, multi-parameter climate proxy records from the Tibetan Plateau (Fig. 1A) and its surrounding areas have enabled reconstructions of climate change and paleo-elevation over geologic (million year) time scales. A large number of stable isotope analyses, particularly  $\delta^{18}\text{O}$  from soil carbonate nodules ( $\delta^{18}\text{O}_{\text{carbonate}}$ ), have been conducted in recent years over the Tibetan Plateau [e.g., Graham et al., 2005, Rowley and Currie, 2006, DeCelles et al., 2007 and Garzzone, 2008]. These  $\delta^{18}\text{O}_{\text{carbonate}}$  observations record the  $\delta^{18}\text{O}$  composition of precipitation ( $\delta^{18}\text{O}_p$ ).

However, interpretations of past climate and the elevation history of the Tibetan Plateau from  $\delta^{18}\text{O}$  records rely upon our understanding of present-day climate- $\delta^{18}\text{O}$  relationships. This study is motivated by deficiencies in our current knowledge of the climate and topographic controls on  $\delta^{18}\text{O}$  across the Himalaya-Tibet region. We provide an analysis of the modern predicted and observed  $\delta^{18}\text{O}_p$  to facilitate future studies that interpret paleo-records of  $\delta^{18}\text{O}$ .

A growing number of recent studies report observed Tibetan  $\delta^{18}\text{O}_p$  and the  $\delta^{18}\text{O}$  composition of surface waters. Observational records in remote regions like the Tibetan Plateau are sparse in both their spatial and temporal coverage. The sparseness of these records inhibit a detailed understanding of the underlying mechanisms for observed variations in  $\delta^{18}\text{O}_p$ . For example, the Global Network for Isotopes in Precipitation (GNIP) includes only one station near Lhasa on the Tibetan Plateau. The Institute of Tibetan Plateau Research in China has established a continuous observation network of  $\delta^{18}\text{O}_p$  on the Tibetan Plateau to augment the Lhasa station [e.g., Tian et al. 1997, Yao et al., 1999, Tian et al. 2003, Tian et al. 2007, Liu et al, 2010]. Observed  $\delta^{18}\text{O}_p$  from this network suggests a strong temperature effect on  $\delta^{18}\text{O}_p$  in the north eastern Tibetan Plateau and strong precipitation amount effects in the central and southern Tibetan Plateau [e.g., Tian et al. 1997, Yao et al., 1999, Tian et al. 2003, Tian et al. 2007, Liu et al, 2010]. In addition, Hren et al. 2009 reported  $\delta^{18}\text{O}$  data from 191 streams across the Himalaya and Tibetan Plateau and suggest that a mixing of moisture sources produced misfits of 1-3km between observed and predicted catchment hypsometric elevations for the water source areas in the central

Tibetan Plateau. Yao et al [2013] summarize  $\delta^{18}\text{O}$  observations from existing precipitation and ice core data in the Tibetan Plateau region and identify three distinct domains of  $\delta^{18}\text{O}$ . These domains include a northern Tibetan Plateau and southern Tibetan Plateau region, with a transition zone in between them. These previous studies document complex spatial and temporal variations in  $\delta^{18}\text{O}$  across the Tibetan Plateau region. However, the limited spatial and temporal resolution of these records, as well as the short record length, inhibit a detailed analysis of the key atmospheric processes influencing  $\delta^{18}\text{O}_p$  across the Tibet Plateau.

Isotope-tracking general circulation models with explicit calculation of stable water isotopes have made advances in predicting  $\delta^{18}\text{O}_p$  as a function of modern, paleoclimatological, and geologic processes [e.g., Armengaud et al., 1998, Hoffmann et al., 1998, Werner et al., 1998; 2011, Cole et al., 1999, and Jouzel et al., 2000]. Such isotope tracking model-based approaches have several advantages over observational approaches for understanding what processes influence water isotopes. These advantages include: 1) simulation of long and continuous records of  $\delta^{18}\text{O}_p$  over a range of timescales (hourly, daily, monthly, yearly, decadal) [e.g., Hoffmann et al., 1998]; 2) availability of corresponding simulated climatological data for identification of the controlling factors of  $\delta^{18}\text{O}_p$ . These data include either diagnostic or derived values such as temperature, precipitation amount, vapor source and transport distance. [e.g. Insel et al., 2013; Jeffery et al., 2012]; and 3) broad spatial coverage in predicted  $\delta^{18}\text{O}_p$  that can be related to land cover and topography [e.g. Feng et al., 2013; Insel et al., 2011; Poulsen et al. 2010]. Thus, while observational approaches are essential for

documenting spatial and temporal patterns in  $\delta^{18}\text{O}_p$ , isotope tracking models provide an important tool for understanding the physical processes associated with observations.

Water isotopes modelling studies of modern and paleo rainfall have been successfully conducted over a range of settings including South America, Western USA, Tibet, and Antarctica. Modeling studies of the Andes and western North America Cordillera [Ehlers and Poulsen, 2009, Poulsen et al., 2010, Insel et al. 2012, Jeffrey et al., 2012, and Feng et al., 2013] find that uplift-induced changes in atmospheric circulation, precipitation, and local mixing conditions could all contribute to changing distributions of  $\delta^{18}\text{O}_p$  across topography and can lead to biases in paleoelevation estimates of hundreds to thousands meters. Vuille and Werner [2005a] investigate the influence of the South American Summer Monsoon (SASM) on  $\delta^{18}\text{O}_p$ , and demonstrated a significant negative association between  $\delta^{18}\text{O}_p$  and SASM over the Amazon basin, SE South America, and the central Andes. Sturm et al. [2007] document the influence of the South Atlantic Convergence Zone on the isotopic composition of precipitation and demonstrate that  $\delta^{18}\text{O}_p$  integrates variations in both precipitation and circulation.

However, water isotope tracking and climate modeling studies of the Tibetan Plateau are limited. Several studies have addressed the effect of the Tibetan Plateau on regional climate. For example, climate modeling studies have documented that surface uplift of the Tibetan Plateau leads to changes in moisture sources and precipitation by affecting the Indian Summer Monsoon, jet stream, and atmospheric

thermostructure [e.g. Ruddiman and Kutzbach, 1989; Boos and Kuang, 2010; Ma et al., 2014]. Previous water isotope modeling studies of the Tibetan Plateau [e.g., Vuille et al. 2005b] investigated the influence of the Asian monsoon on  $\delta^{18}\text{O}_p$  using the ECHAM4-wiso atmospheric model and found that variations in the amount of precipitation provide a first-order negative relationship with  $\delta^{18}\text{O}_p$ , and also that  $\delta^{18}\text{O}_p$  variations in this region are sensitive to fluctuations in the Asian monsoon intensity. Gao et al. [2015] applied empirical orthogonal functions from the  $\delta^{18}\text{O}_p$  outputs of the LMDZiso model and reconstructed annual  $\delta^{18}\text{O}_p$  data with a  $2.5 \times 3.75$  degree resolution over the Tibetan Plateau. He et al. [2015] used a combination of in situ measurements with satellite data and atmospheric general circulation modeling. They revealed that the atmospheric convective activity over the Indian continent correlated with the summer precipitation isotopologue composition over southern Tibet. Based on the previous work, the various factors which can influence  $\delta^{18}\text{O}_p$  can be summarized as: (1) temperature (temperature effect) and changes of the atmospheric thermostructure, (2) precipitation (amount effect) and changes of the precipitation scheme, and (3) changes in vapor sources and atmospheric circulation.

In this study, we complement previous work by using an isotope tracking global atmospheric general circulation model (GCM) to estimate modern  $\delta^{18}\text{O}_p$  variations across the Tibetan Plateau. Our emphasis is on regional scale variations in  $\delta^{18}\text{O}_p$  that emerge from analysis of the 30 year predicted climatology. The model is forced with the present day boundary conditions including: sea surface temperatures, greenhouse gas concentrations, and orbital boundary conditions. Model results are

used to identify the physical processes responsible for these variations based on a 30 years model simulation. The questions addressed in this manuscript include: (1) how well does ECHAM5-wiso agree with newly available observations (2) what processes control the minimum/maximum daily  $\delta^{18}\text{O}_p$  values over the Tibetan Plateau, and (3) how well does a simplified 1D Rayleigh Distillation Model (RDM) of predicted  $\delta^{18}\text{O}_p$  across the Himalaya topography compare to GCM-derived estimates? This study presents an analysis of predicted  $\delta^{18}\text{O}_p$  variations that compliment spatially and temporally limited observations of  $\delta^{18}\text{O}_p$ . Our documentation of these variations has potential benefit for geoscience studies investigating paleo, proxy records of  $\delta^{18}\text{O}_p$  preserved in the sedimentary record that are limited in their understanding  $\delta^{18}\text{O}_p$  variability across the plateau.

## 2. Methods

### 2.1 The ECHAM5-wiso isotope-enabled GCM

ECHAM5 is the fifth version of an atmospheric general circulation model designed to simulate climate. A full description of the ECHAM5 model and its formulation can be found in Roeckner et al. [2003]. The ECHAM5-wiso model is an enhanced version of ECHAM5 with the added ability to simulate isotope composition in precipitation. Water isotopologues ( $\text{H}_2^{16}\text{O}$ ,  $\text{H}_2^{18}\text{O}$  and HDO) undergo kinetic and equilibrium fractionation during the phase transitions in the atmosphere, and are treated as independent tracers (for details, see Hoffmann et al. [1998] and Werner et al. [2011]). Its performance has been evaluated in several publications [Werner et al. 2011, Langebroek et al., 2011 and Butzin et al., 2014] that demonstrate agreement of



the simulated isotopic fraction of precipitation with observational data both on a global and regional scale. Yao et al [2013] evaluated the application of different isotope tracking approaches (including ECHAM5-wiso) over the Tibetan Plateau, and suggested that high-resolution atmospheric models capture the temporal and spatial distribution of  $\delta^{18}\text{O}_p$  and its relationship with vapor transport.

## 2.2 Model setup and boundary conditions

An ECHAM5-wiso simulation was conducted for modern conditions at a T63 spectral resolution (equivalent to a grid spacing of  $\sim 1.9$  degrees or  $\sim 200$  km in latitude and longitude), and L19 vertical resolution (19 vertical levels up to 10hPa). Figure 1B shows the Tibetan Plateau topography at 1km and T63 resolution. A comparison of these figures shows that T63 topography does not represent individual mountain ranges, but rather only the long wavelength topographic features. The simulation was forced with present-day boundary conditions including the Atmospheric Model Intercomparison Project 2 (AMIP2) sea surface temperature and sea ice data from 1957-2000 and observed greenhouse gas concentrations for the same period [Nakicenovic et al, 2000]. The simulation was conducted for  $> 40$  model years. A climatological reference period of 30 years was established for the analysis presented here using the simulation years 1970-1999. The  $\delta^{18}\text{O}$  of soil water often requires a longer equilibrium time due to the greater heat capacity of soil and thus longer equilibrium time. Since the isotopes are not tracked on land (e.g. for soil wetness), the model spin-up time for the atmosphere and  $\delta^{18}\text{O}_p$  to equilibrate was less than 2 years.

### 2.3 Lagrangian trajectory analyses

Spatial variations in the water isotope fraction occur across the world [Bowen and Revenaugh, 2003]. Vapor originating from different source regions contains different isotope ratios and therefore influences  $\delta^{18}\text{O}_p$  of the target regions where precipitation occurs. However, the  $\delta^{18}\text{O}_p$  of a target region is not only influenced by the water isotopic fraction of the source region, but also by other processes such as moisture convection, vapour transport distance, and the climate condition along the vapour transport path.

Lagrangian trajectory analysis is a method of defining air mass trajectories and source regions. In this study, the backward trajectories of winds that deliver precipitation are approximated in a 3D terrain-following pressure level system referred to as hybrid sigma pressure levels. A schematic of the hybrid sigma-pressure levels used in this study is shown in Figure 2. The hybrid sigma pressure level approach uses a terrain-following pressure level system that enables tracking of moisture advection from below the plateau onto the Tibetan Plateau. This hybrid sigma pressure level approach is preferred over using fixed pressure levels because of the large topographic variations between the low lands surrounding the Tibetan Plateau and the Plateau itself. For example, a trajectory analysis conducted at a constant pressure of 900hpa would not allow calculation of back trajectories from the plateau (at a much lower pressure) to the vapor source. Large scale tropical convection is not only influenced by moisture vapor near the surface but also aloft

(Sherwood et al. 2010). Given this, our trajectory analysis was conducted at three atmospheric levels. These levels span from the Earth's surface to 300hpa and include (Fig. 2): 1) a surface level; 2) a boundary level; and 3) a middle troposphere level.

The wind fields in the previous three hybrid sigma pressure levels are integrated within each of the three levels for the calculation. The three hybrid sigma pressure levels used in this study are composed of model hybrid sigma pressure levels 19-11. Thus, 3 model levels are grouped into each of the 3 atmospheric levels used (Fig. 2) in our back trajectory analysis. For the backwards tracking, we start from one coordinate, and check the average u and v wind velocities at this coordinate, and calculate where an air parcel of this target location was in the previous time increment (20mins). Following this, we determine the wind speed of the new location at that time step, and track it backwards one time step further, etc. This procedure was repeated until the 10-day path of the trajectory is determined.

One Limitation of this approach is that it does not strictly follow water parcels or account for mixing, or precipitation along a pathway. Despite this limitation, the backward trajectory technique used here provides insight into the vapor path and source of precipitation for winds in the lower troposphere in a region of high topographic variation.

A brief summary of the Lagrangian back trajectory calculation is provided here. A more detailed description is available in Betto [2005]. A differential equation for the trajectory analysis is defined to describe the trajectory of a specific infinitesimally small air parcel:

$$\frac{dX}{dt} = X[\dot{X}(t)] \quad (1)$$

Where  $t$  is time,  $X$  is the parcel position at time  $t$  and  $\dot{X}$  is the velocity vector at time  $t$ . Using a short integration time step, the solution of equation (1) can be solved numerically to a second order:

$$X(t_1) = X(t_0) + (\Delta t) \left. \frac{dX}{dt} \right|_{t_0} + \frac{1}{2} (\Delta t)^2 \left. \frac{d^2X}{dt^2} \right|_{t_0} + \dots \quad (2)$$

The trajectories are calculated in this study using the ‘real time’ simulated 6-hour u- and v-components of the wind velocity field, rather than the long-term mean wind fields from the model outputs. The 6-hour wind velocity field was linearly interpolated in each pressure level to a 20-minute time interval. The wind vectors at a target location inside the T63 resolution grid box were interpolated using a bilinear interpolation. The trajectories were calculated for ten days prior to January 15<sup>th</sup> and August 15<sup>th</sup> for each of the 30 simulation years for the results presented in section 3.3. The 15<sup>th</sup> day was chosen because it is the mid-point of months within different seasons.

Extreme values in  $\delta^{18}\text{O}_p$  are discussed in section 4.3 and back trajectories for these were calculated for the days prior to extreme events. The wind (east-west wind and south-north wind) field of those three representative atmospheric levels is

averaged from the corresponding model hybrid sigma-pressure levels and used for the trajectory calculation.

## 2.4 Rayleigh Distillation Model (RDM) of Adiabatic Condensation

The RDM modelling approach is a simplified approach used to predict water isotope fractionation in many paleoproxy interpretation studies (e.g. Rowley and Garzzone). In this study we compare the RDM approach to the more sophisticated ECHAM5-wiso predicted  $\delta^{18}\text{O}_p$  to evaluate under what conditions the RDM approach is justified. The motivation for this two model comparison is to evaluate if the RDM (adiabatic processes) agree with GCM predictions that account for both adiabatic and diabatic atmosphere processes. The simpler RDM calculates the condensation and change in isotopic composition of a single air parcel during adiabatic cooling. It tracks water vapor content, and the condensate isotopic fraction of a single near-surface air parcel as it ascends over topography, thereby providing the precipitation isotopic fraction as a function of elevation. In contrast, the ECHAM5-wiso GCM accounts both adiabatic and diabatic hydrological processes. Water isotopologues are allowed to undergo equilibrium and kinetic fractionation during phase changes in the atmosphere.

The RDM approach used in this study follows that of Rowley and Garzzone [2007] and Feng et al. [2013]. The RDM model is based on the conservation of moist static energy. As an unsaturated air parcel ascends it cools at a dry adiabatic lapse rate until its temperature decreases to the dew point and then cools at the moist adiabatic lapse rate. The temperature and altitude curve can be modeled and the remaining

vapor fraction  $f$  can be calculated from the saturation vapor pressure that depends on the temperature. The delta value of remaining vapor and condensation can then be calculated as:

$$(\delta^{18}O_v)_j = ((\delta^{18}O_v)_{j-1} + 1000)f^{(\alpha-1)} - 1000 \quad (3)$$

$$(\delta^{18}O_l)_j = \alpha((\delta^{18}O_v)_j + 1000) - 1000 \quad (4)$$

where  $j$  is the  $j^{\text{th}}$  elevation level,  $l$  is for the condensed vapor,  $v$  is the remaining vapor,  $\alpha$  is the fractionation factor and can be calculated using the method of Majoube [1971] for liquid-vapor equilibrium. Condensation is assumed to be equal to precipitation in the RDM.

The initial condition of the RDM calculation ( $\delta^{18}\text{O}$  in the water vapor, relative humidity and temperature) are driven from the GCM outputs. The GCM-derived RDM initial conditions are averaged from the GCM model outputs for the monsoon season at the Himalaya front (84°E-92°E, 23°N-30°N). The RDM  $\delta^{18}\text{O}_p$  is calculated starting with a GCM-derived moisture source at low elevation (the foreland of the Himalaya). The GCM simulated  $\delta^{18}\text{O}_p$  with elevation is then compared to the RDM prediction to evaluate the difference between the approaches over the large elevation gradient of the Himalaya.

## 2.5 Analysis of $\delta^{18}\text{O}$ mixing

An assumption of the RDM model is that an air parcel is isolated and has no exchange with its surroundings. In reality this assumption may not always be valid. Analysis of  $\delta^{18}\text{O}$  mixing in a GCM [e.g. see Feng et al. 2013] can be used to evaluate the extent to which  $\delta^{18}\text{O}$  mixing affects  $\delta^{18}\text{O}_p$  values. Using model estimated three-dimensional wind-fields and vapor  $\delta^{18}\text{O}$  fields as inputs, the temporal difference of the  $\delta^{18}\text{O}$  of equilibrium condensate ( $\delta^{18}\text{O}_c$ ) due to flow in three directions (latitudinal, longitudinal and vertical) can be estimated by equation 5. For this calculation, the  $\delta^{18}\text{O}_l$  in equation 4 is assumed to be the same as  $\delta^{18}\text{O}_c$  under the assumption that all condensate vapor produces precipitate.

$$\frac{\partial \delta^{18}\text{O}_c}{\partial t} \sim -\vec{V} \cdot \vec{\nabla} \delta^{18}\text{O}_v \quad (5)$$

where  $V$  is the wind vector in the three directions. By assuming immediate condensation of advected vapor and using the fraction factor  $\alpha$  [Majoube 1971] for liquid vapor equilibrium, the  $\delta^{18}\text{O}$  mixing rate can be calculated from:

$$\vec{V} \cdot \vec{\nabla} \delta^{18}\text{O}_c = \vec{V} \cdot \vec{\nabla} \delta^{18}\text{O}_v + \vec{V} \cdot \vec{\nabla} T \left( -\frac{6.7123 \times 10^3}{T^2} + \frac{3.3328 \times 10^6}{T^3} - \frac{1.05123 \times 10^9}{T^4} \right) \quad (6)$$

The analysis of  $\delta^{18}\text{O}$  mixing provides the upper limit but not the actual value for two reasons: 1) This method assumes full condensation of the advected vapor. And 2) the  $\delta^{18}\text{O}$  mixing is calculated for the monsoon season (July-September) when vapor content and precipitation amounts are the largest in the Tibetan Plateau region.

### 3. Results

In the following sections we present results for 1) model-simulated temperature, precipitation, and  $\delta^{18}\text{O}$ ; 2) spatial and temporal variations in simulated  $\delta^{18}\text{O}$  and 3) vapor source analyses based on the trajectory and zonal winds.

#### 3.1 Model Validation and Seasonal plots of Tibetan Plateau temperature, precipitation, wind and $\delta^{18}\text{O}_p$

The Himalaya and Tibet regions have two distinct seasons including a dry (winter) and a wetter (summer) season. The simulated temperature and precipitation has been compared and validated with previous modeling studies and reanalysis data from across the Tibetan Plateau. The results show an agreement that is within the differences between the ERA40 and NCEP reanalysis data. This comparison is presented in Mutz et al. [2016] using the same resolution ECHAM5-wiso model outputs as this study. Thus, the model resolution used in this study agrees with reanalysis data as well as the different reanalysis data sets agree with each other [Mutz et al., 2016]. Furthermore, our study uses a T63 resolution ECHAM5 model. A lower resolution (T42) version of ECHAM has already been used and validated for climate studies [Battisti et al., 2014; Roe et al., 2016]. More specifically, Battisti et al. [2014] provide a comparison of simulated and observed precipitation, and also report a good agreement with stalagmite proxy records. Roe et al. [2016] conducted a limited set of simulations at higher resolution but found no significant differences



from the lower resolution analysis. Finally, Werner et al. [2011] and Yao et al. [2013] suggested a higher model resolution provides better results on smaller scale (mainly due to a better resolved topography) but doesn't result in large changes of the general temperature, precipitation, and  $\delta^{18}\text{O}_p$  patterns such as we interpret from the model results in this manuscript.

Figure 3 shows the 30-year climatologies of the winter (defined as DJF) and summer (defined as JAS) seasons, and the difference between summer and winter season (JAS-DJF). In the winter, there is small amount ( $< 4$  mm/day) of precipitation across the Tibetan Plateau (Fig. 3A). In summer (Fig. 3B) precipitation rates are  $< 4$  mm/day in NW Tibet but significantly higher over the Himalaya ( $\sim 20$  mm/day) and most of the SE Plateau ( $\sim 10$  mm/day). There is less precipitation (0-4 mm/day) in NW Tibet but more precipitation (increasing from 0-4 mm/day in the middle of Tibet to  $> 10$  mm/day over SE Tibet) in the summer than in winter (Fig.3C). The mean surface temperature is about  $-25^\circ\text{C}$  in NW Tibet and  $-15^\circ\text{C}$  in SE Tibet in the winter (Fig. 3D), and increases to around  $0^\circ\text{C}$  across Tibet in the summer (Fig. 3E). The mean summer and winter temperature difference increases from south to north across Tibet from around  $0^\circ\text{C}$  to  $20^\circ\text{C}$  (Fig.3F). Analysis of the seasonality of the Tibetan Plateau surface winds also illustrates two distinct patterns. Strong westerly winds prevail in the winter (Fig.3G). In summer, southeasterly winds associated with the Indian monsoon system arrive in the Himalaya (Fig.3H).

Summer and winter differences in  $\delta^{18}\text{O}_p$  (precipitation-weighted mean) is also present. In the winter, spatial variations in  $\delta^{18}\text{O}_p$  are  $\sim 5\%$  over the Tibetan Plateau

(Fig. 4A), whereas in the summer, the  $\delta^{18}\text{O}_p$  distribution shows a distinct northwest-southeast spatial gradient decreasing from  $\sim -5\text{‰}$  in NW Tibet to  $\sim -20\text{‰}$  in SE Tibet (Fig. 4B). The seasonal difference (JAS-DJF) in  $\delta^{18}\text{O}_p$  is  $> +6\text{‰}$  in the NW Tibetan Plateau and  $< -6\text{‰}$  in the SE Tibetan Plateau (Fig.4C). Different from the zonal distributions in  $\delta^{18}\text{O}_p$  are observed in previous studies [e.g. Tian et al. 1997 and Yao et al. 2013], the three zones extend from the SE to the NW (as indicated with white dash lines in Fig. 4C), rather than from south to north. This information is important for paleoclimatology and paleo altimetry studies when interpolating proxy data for the Tibetan Plateau. This SE to the NW direction of  $\delta^{18}\text{O}_p$  zones and the climate controls on it have been independent of this study identified by a cluster analysis of  $\delta^{18}\text{O}_p$  [Mutz et al. 2016]. The standard deviation ( $\sigma$ ) in  $\delta^{18}\text{O}_p$  was calculated from 90 monthly means of predicted  $\delta^{18}\text{O}_p$  (30 simulation years  $\times$  3 month in a season). The winter  $\sigma$  in  $\delta^{18}\text{O}_p$  values vary between  $\sim 2$  to  $4.5\text{‰}$  in south-central Tibet (Fig.4D). The  $\sigma$  of summer  $\delta^{18}\text{O}_p$  is  $\sim 2$  to  $4.5\text{‰}$  in central Tibet (Fig.4E). The summer-winter difference (JAS-DJF) in the  $\sigma$  of  $\delta^{18}\text{O}_p$  is most positive in northern Tibet and most negative in southern Tibet (Fig.4F). In the following sections we simplify our presentation by focusing on January and August as representative months for the winter and summer. These months were selected for the back-trajectory analysis which requires high-resolution (20 minute) wind velocities.

### 3.2 Thirty-year spatial and temporal variations in $\delta^{18}\text{O}$

Spatial and temporal variations in  $\delta^{18}\text{O}_p$  are presented for two profiles across the Tibetan Plateau (white lines in Figure 4A and B) and for 6 selected locations (black dots and letters in Fig. 4D-E which represent cities, significant geographic features such as lakes, or published proxy-data sample locations). In this section, we focus on a statistical analysis of the daily time series for the six selected locations: Location A and B from the middle transition zone, location C, D and E from the southeast zone and location F from the northwest zone (Fig. 4D). The environmental controls of  $\delta^{18}\text{O}_p$  are discussed in Section 4.

Strong variations in mean daily  $\delta^{18}\text{O}_p$  are observed in January and August over the 30 year simulation duration in all six selected locations on the Tibetan Plateau (Fig. 5, 6, 7). In these Figures, monthly values are presented and include the maximum and minimum daily  $\delta^{18}\text{O}_p$ , mean daily  $\delta^{18}\text{O}_p$  (dashed lines), and  $\pm 1\sigma$  (standard deviation) from the mean  $\delta^{18}\text{O}_p$  value (boxes). Two general patterns are evident. First, large variations in the daily mean  $\delta^{18}\text{O}_p$  are present and range from  $\sim -25$  to  $+5$  ‰. These daily variations agree well with the results of Liu et al. [2010] that reported a daily variation of  $-28.7$  ‰ to  $-7.8$  ‰ based on 70 daily measurements of  $\delta^{18}\text{O}_p$  in the year 2000 at Nague (31.48N, 92.06E) in the central Tibetan Plateau. Second, large interannual variations are also present for each area; the standard deviation of the 30 year precipitation-weighted annual  $\delta^{18}\text{O}_p$  data is about 1.2 - 3.5 ‰ for all sites.

The different regions on the Tibetan Plateau demonstrate different seasonal trends in  $\delta^{18}\text{O}_p$ . In the middle zone of the Tibetan Plateau (locations A, B; Figs. 4B

and 5), Low mean monthly  $\delta^{18}\text{O}_p$  ( $\sim -15\text{‰}$ ) is present in the winter (Figs. 5A and C) and higher  $\delta^{18}\text{O}_p$  ( $\sim -10\text{‰}$ ) is found in summer (Figs. 5B and D). However, the seasonal differences in mean monthly  $\delta^{18}\text{O}_p$  at each location are 5 ‰ (Figs. 5A-B and C-D). Daily  $\delta^{18}\text{O}_p$  variations in the middle zone are much higher in the summer than in winter.

In the southeast zone (location C, D and E, Fig. 4B, Fig. 6), there is more precipitation than the other zones due to the stronger influence of the monsoon system (Figs. 3A-B). The different precipitation distribution in this zone results in the  $\delta^{18}\text{O}_p$  having an opposite seasonality to that of the other zones. More specifically, the precipitation events in the southeast zone (Fig. 6) have higher  $\delta^{18}\text{O}_p$  in the winter and lower  $\delta^{18}\text{O}_p$  in the summer compared to the other zones (Figs. 5 and 7). This trend could be caused by the high summer rainout amount. The seasonality of  $\delta^{18}\text{O}_p$  across the southeast zone varies from 10 ‰ at location C (Figs. 6A and B) to 3 ‰ at location E (Figs. 6E and F).

At location F, the mean daily  $\delta^{18}\text{O}_p$  is about -16 ‰ in the winter and about -5 ‰ in the summer (Fig. 7). High  $\delta^{18}\text{O}_p$  in summer and low  $\delta^{18}\text{O}_p$  in winter are correlated with the high temperature in summer and low temperature in winter which reflects a 'temperature effect' influence on the  $\delta^{18}\text{O}_p$  variation.

North-south and west-east variations in  $\delta^{18}\text{O}_p$  are presented along two profiles in Figure 8. The following points are evident. First, seasonal differences in the spatial distribution of  $\delta^{18}\text{O}_p$  are present. For example,  $\delta^{18}\text{O}_p$  values have a lower spatial variation ( $\pm 5$  ‰) in the winter on the Tibetan Plateau, (Fig. 8A B and C), but a large

spatial difference ( $\pm 10\text{‰}$ ) is seen in the August  $\delta^{18}\text{O}_p$  values (Fig.8D, E, and F).

Second, minimum  $\delta^{18}\text{O}_p$  occurs at different locations on the plateau for each season.

The north-south cross section (Fig. 8B, E) indicates the minimum in  $\delta^{18}\text{O}_p$  ( $\sim -19\text{‰}$ ) is

found on the north of the Tibetan Plateau in January (Fig.8B) and migrates to the

south of the Tibetan Plateau in August ( $\sim -20\text{‰}$ ) (Fig.8E). The west-east cross-section

also shows a season shift in  $\delta^{18}\text{O}_p$  values (Fig. 8C, F). Minimum  $\delta^{18}\text{O}_p$  occurs on the

west side of the Tibetan Plateau in January ( $\sim -17\text{‰}$ )(Fig.8C), and migrates to the east

in August ( $\sim -20\text{‰}$ ) (Fig.8F). Third, similar  $\delta^{18}\text{O}_p$  and isotopic lapse rates of  $\sim -3.1$

$\text{‰/km}$  are present in the Himalaya and southern Tibetan Plateau for both seasons (Fig

8B and E). In contrast, the western side of the Tibetan Plateau has a lapse rate of  $\sim -3.4$

$\text{‰/km}$  in the winter (Fig 8C) that decreases to  $-1.7\text{‰/km}$  in the summer (Fig.8F).

These results indicate that seasonal variations in  $\delta^{18}\text{O}_p$  are present, but spatially

variable in their magnitude across the Himalaya and Tibetan Plateau.

### 3.5 vapor source analysis based on trajectory analysis and zonal winds

Results from the Lagrangian trajectory analysis are presented here to assess how seasonal variations in the vapor source influence predicted  $\delta^{18}\text{O}_p$  values.

Trajectories were computed for 10-days prior to January 15<sup>th</sup> and August 15<sup>th</sup> of the

30 simulation years (Fig. 9, 10). Location F in the northeast and location C in the

southeast are presented as representative examples for vapor transport at the three

hybrid sigma pressure levels (Section, 2.3, Fig. 2, surface level, boundary level and

middle troposphere level). Trajectories show localized circulation at the surface layer

which represents an inversion that would tend to prevent strong mixing from aloft, and a prevailing westerly pathway in the boundary layer and mid-troposphere in January (Fig. 9). The trajectories for these locations track predominantly westerly winds from the western arid region to the Tibetan Plateau.

August trajectories for the same locations on the Tibetan Plateau show a different pattern than for January (Fig. 10). Location C is strongly influenced by the monsoon system in August (Fig. 10 E-F) such that most vapor originates from the Indian Ocean. In contrast, vapor at location F is more heavily influenced by the west winds and back trajectories lead to either the NW or SW of the Tibetan Plateau (Fig. 10 C). A second prominent feature of the rainy season is that dry air is sourced from the west in the middle troposphere (Fig. 10D). These results are consistent with those with those of Hren et al. [2009], who found that the monsoon-derived moisture is progressively mixed with central Asian air masses in the western and northern parts of the Tibetan Plateau.

#### 4. Discussion

In the following sections we discuss the results in the context of: (1) a comparison of GCM predictions and observations (precipitation and stream water  $\delta^{18}\text{O}$ ), (2) the causes for the extreme values in  $\delta^{18}\text{O}$ ; and (3) application of the RDM at the Himalayan front.

#### 4.1 Predicted and observed precipitation $\delta^{18}\text{O}$ comparison

The performance of the ECHAM5-wiso predicted 30-year average  $\delta^{18}\text{O}_p$  are compared to observations to evaluate the model performance. Two years of observational  $\delta^{18}\text{O}_p$  data were available for comparison from Tian et al. [2007]. A 30-year model predicted average  $\delta^{18}\text{O}_p$  was compared to individual years of observations to assess if the individual observations occur within the range of model predicted values. The locations of observed  $\delta^{18}\text{O}_p$  studies are shown in Figure 4C and individual station locations were compared to simulations using a bilinear interpolation of model grid cells to each location (Fig. 11). Overall, a good agreement is present between predicted and observed values. Model predictions successfully produce seasonal variations in  $\delta^{18}\text{O}_p$  at several locations (e.g. Figs. 11A, B, F, G, H). However, differences between predicted and observed values are present. Large ( $> 2\sigma$  of the model 30 year outputs) differences between the model and observation are found at Shiquanhe and Yushu (Figs. 11 C and E). For example, the model  $\delta^{18}\text{O}_p$  prediction for the northwestern Tibetan Plateau is higher than observations during the winter and spring (Figs. 11 C, D, F, G and H). These differences could result from several factors. First, the differences might suggest an influence of topographic effects on  $\delta^{18}\text{O}_p$  at Shiquanhe and Yushu that are not present in the model due to its resolution. Second, there is a model bias of overestimating of  $\delta^{18}\text{O}_p$  during the winter in the westerly region. And third, the two years of  $\delta^{18}\text{O}_p$  observational data used in this comparison deviate by two-to-three standard deviations from the the 30-year climatological averages thereby allowing for the possibility that extreme variations

from the mean were measured in those years (Figs. 11 C - E). More observations from these locations are needed to differentiate between the above explanations.

#### 4.2 Predicted and observed streamwater $\delta^{18}\text{O}$ comparison

Previous work by Hren et al [2009] presented  $\delta^{18}\text{O}$  from stream waters ( $\delta^{18}\text{O}_{\text{water}}$ ) at  $\sim 30^\circ\text{N}$  and  $\sim 86^\circ\text{E}$  that were intermittently measured from 1998 to 1999. Stream water can reflect mean annual precipitation weighted variations in  $\delta^{18}\text{O}_p$  [Yurtsever and Gat, 1981] and motivates presentation of the GCM predicted mean annual  $\delta^{18}\text{O}_p$  (Fig. 12). Simulated  $\delta^{18}\text{O}_p$  was plotted at the same observational cross section (Figs. 12 C and D). Simulated and observed  $\delta^{18}\text{O}$  agree well along both the west-east cross section R-R' (Fig. 12C) and the north-south cross section P-P' (Fig. 12D). The north-south cross section shows that  $\delta^{18}\text{O}_p$  decreases from south to north across the Himalaya and increases on the Tibetan Plateau from south to north (Fig. 12D, see also August results in Fig. 8E). ECHAM5-wiso  $\delta^{18}\text{O}_p$  is higher than the  $\delta^{18}\text{O}_{\text{water}}$  at the west end of Himalaya by about 4 ‰. Although this difference is comparable to the model simulated interannual variability of  $\sim 4\text{-}6$  ‰ (Fig. 12), the observations at the west end of the Himalaya are more negative than the model predicted values. Possible causes for the remaining disagreement could include: (1) there is a mixing of surface waters with more isotopically depleted sources such as a stream source from a higher altitude that flows down to the sample site; (2) the west-east  $\delta^{18}\text{O}_{\text{water}}$  at the west of the Himalaya represents a local signal influenced by the catchment topography that cannot be reproduced by the GCM due to the coarser



model resolution (e.g. Fig. 1); (3) the observational duration of Hren et al, (2009) is relatively short (1 year) compared to the 30 year climatological values predicted, and (4) a systematic west to east bias in model predictions. Concerning the last point, comparisons of model results to other  $\delta^{18}\text{O}_p$  data (see section 4.1) are in agreement and suggest the first three points are the more likely explanation.

#### 4.3 Causes for extreme values in $\delta^{18}\text{O}_p$

Our results indicate that the range of daily  $\delta^{18}\text{O}_p$  values is as large as 25 - 30 ‰ (Fig. 5-7, see also Liu et al. 2010). To investigate possible explanations for the range of daily  $\delta^{18}\text{O}_p$  values in the 30 simulation years (total number of days analyzed = 30 years  $\times$  31 days = 930) for each month are characterized into 3 groups: (1) days with extreme highs in  $\delta^{18}\text{O}_p$  values (daily value  $>$  95 percentile of the  $\delta^{18}\text{O}_p$ ), (2) days with extreme low  $\delta^{18}\text{O}_p$  values (daily value  $<$  5 percentile of the  $\delta^{18}\text{O}_p$ ), and (3) days with mean  $\delta^{18}\text{O}_p$  values (average  $\delta^{18}\text{O}_p$  value  $\pm$  0.5 ‰) as a reference. The conditions (temperature, precipitation and vapor sources) of those days in the three groups are analyzed for January and August at representative locations.

The average temperature and precipitation for the three groups and their standard deviations are summarized in Table 1. An increase in the precipitation amount corresponds with a decrease in  $\delta^{18}\text{O}_p$  at most of the locations for both January and August, but there are no systematic correlation between the changes in  $\delta^{18}\text{O}_p$  and changes in the precipitation amount. For example, daily extreme precipitation ranges from 6.9 mm/day in January to 54.5 mm/day at location D during August,

corresponding to values for  $\delta^{18}\text{O}_p$  of -2.0 ‰ and -21.5 ‰. In contrast, daily extreme precipitation range from 0.57 to 2.78 mm/day at location F during January, corresponding to values for  $\delta^{18}\text{O}_p$  of -6.2 ‰ and -30.0 ‰. We find that the temperature differences between the groups are small, with a maximum of 3 °C and minimum of 0.1°C between the days with extreme high  $\delta^{18}\text{O}_p$  values and extreme low  $\delta^{18}\text{O}_p$  values. For the three groups, there is no significant correlation between temperature and  $\delta^{18}\text{O}_p$ . Finally, large daily variations in temperature and precipitation exist within the same extreme  $\delta^{18}\text{O}_p$  group. Extreme  $\delta^{18}\text{O}_p$  values do not systematically correspond with either precipitation or temperature extremes.

Apart from temperature and precipitation, vapor source can also significantly influence  $\delta^{18}\text{O}_p$ . Backwards trajectory analyses were conducted to determine changes in the vapor source for the extreme event days in the above three groups at location C and location F during the months of January and August (Fig. 13). Orange, blue, and green lines in Fig. 13 represent backward trajectories for days with extreme high, mean, and extreme low  $\delta^{18}\text{O}_p$  values. The surface layer is not relevant for diagnosing the vapor sources outside the Tibetan region in January for the northwest region of the Tibetan Plateau (Fig. 9). Given this, the surface layer trajectories for January are not shown here. Results show a clear vapor source variance for the extreme events (Fig. 13). For example, at location C during August the northeast and southwest vapor sources (orange color) correspond with the extreme high  $\delta^{18}\text{O}_p$  values, and vapor from the Indian Ocean (blue and green color) correspond with mean and extreme low in  $\delta^{18}\text{O}_p$  (Figs. 13 E and F). The difference in the  $\delta^{18}\text{O}_p$  values within a group could be a

result of the rainout from persistent precipitation. Vapor originating from west of the Arabian Sea in August corresponds with extreme high  $\delta^{18}\text{O}_p$  values (Figs. 13 B and E). The reasons could be that vapor sources from the ocean in the tropical region have a higher  $\delta^{18}\text{O}$  value than the continental sources in the mid-latitude. Furthermore, a clear difference in the vapor source is found during January for location F (Fig. 13A). The extreme low and mean  $\delta^{18}\text{O}_p$  values at location F originate from the west, the vapor for extreme high  $\delta^{18}\text{O}_p$  values at location F originates from the Indian continent. Different from the above results, there are also rare cases in which a northwest vapor source coincides with extreme low  $\delta^{18}\text{O}_p$ , and the Indian Ocean vapor source coincides with extreme high  $\delta^{18}\text{O}_p$  (e.g. Fig. 13 D). In these cases, other factors other than the vapor source play a more important role.

#### **4.4 Comparisons of the Rayleigh Distillation Model (RDM) to the Tibetan Region GCM simulations**

The surface elevation history of the Himalaya-Tibet region is widely studied due to its importance as the largest orogenic plateau on Earth and allows for the study of climate and tectonic interactions. Applications of the RDM in paleo altimetry studies [e.g. Rowley and Garzzone 2007] has been preferred and widely used for interpreting modern and paleo  $\delta^{18}\text{O}_p$  observations because of the complexity and time consuming nature of conducting GCM simulations. In this section, GCM simulated  $\delta^{18}\text{O}_p$  and  $\delta^{18}\text{O}_p$  predicted by a RDM (forced with GCM output) was compared along one profile up the Himalaya front (averaged between 86 and 94 °E) during the

monsoon season (JAS). The initial conditions for the RDM are prescribed based on the GCM. The GCM derived initial conditions for the RDM include the initial vapor temperature ( $T_s$ ) 28.4 °C, initial vapor specific humidity ( $q_s$ ) 16.8 g/kg, and initial vapor  $\delta^{18}\text{O}_v$  of -13.0 ‰ (Fig. 14A).

The two modeling approaches show an agreement whereby GCM  $\delta^{18}\text{O}_p$  differs from the RDM predictions near the surface, and at ~2km and >4km elevation. The maximum difference between the two approaches in Figure 14A is < 1‰, which is notably less than the difference of > 3‰ observed in the North American cordillera region [Feng et al. 2013]. Feng et al. [2013] evaluated the non-Rayleigh influences on the  $\delta^{18}\text{O}_p$  in and around the North American cordillera, and demonstrated the significant influence of atmosphere processes on  $\delta^{18}\text{O}_p$  including shifts in local precipitation types (e.g. from precipitation to snow, or from large scale precipitation to convective precipitation), development of air mixing, low-level vapor recycling (defined as the ratio of the evaporation to the precipitation), and changes in the vapor source. Among these atmosphere processes, the low-level vapor recycling south of the Himalaya is about 10-30% which has no significant influence on the RDM calculation. The precipitation type is assumed to not change during the monsoon season. The difference between the Himalaya and North American cordillera is likely due to the weaker upslope flow in Tibet and the higher specific humidity of monsoonal air parcels compared to air parcels over North America. As seen in Fig. 14B, the airflow is blocked at the Himalaya front, forming a vertical cell. This amount of upslope flow can not contribute to high-altitude mixing along the flanks

[Galewsky 2009]. Analyses of the upper limits of the mixing rate support this conclusion (Fig.14B). For example, the  $\delta^{18}\text{O}_p$  mixing rate exchange of an air parcel with the surrounding environment is  $< 0.2 \text{ ‰}$  across the Himalaya (Fig.14B), which suggests that the parcels undergo less mixing when convection is strong. The comparison between the RDM and GCM in this study suggests that the adiabatic process is the main control on  $\delta^{18}\text{O}_p$  at the Himalaya topographic front during the monsoon season. Our findings support the use of the RDM for modern conditions across the Himalaya front. However, this result may not be applicable to other regions neighboring Tibet and evaluation of the RDM approach for other locations and for paleo conditions when topography or wind trajectories may significantly differ requires additional verification.

## 5. Conclusions

The main conclusions drawn from this study are:

(1) Agreement exists between model-simulated  $\delta^{18}\text{O}_p$  and 2 years of observations on the Tibetan Plateau [Tian et al, 2007]. This conclusion confirms the overall good performance of the ECHAM5-wiso for the Tibetan Plateau region. The simulations also successfully predicted simulated seasonal trends in  $\delta^{18}\text{O}_p$  for different zones. Disagreements are noticeable in the model's overestimation of  $\delta^{18}\text{O}_p$  during the winter in the western Tibetan plateau.

(2) Large daily  $\delta^{18}\text{O}_p$  variations of  $-25$  to  $+5 \text{ ‰}$  are documented for the 30 simulation years across the region as well as seasonal variation of  $5$  to  $10 \text{ ‰}$ , and

interannual variation of 1.2 to 3.5 ‰. This result suggests caution should be taken when interpreting short-term (from season to season, or between years)  $\delta^{18}\text{O}_p$  observations as representative of climatic conditions ( $\geq 30$  years).

(3) Our results are at odds with previous studies that define north-to-south  $\delta^{18}\text{O}_p$  distribution zones [Tian et al. 2007 and Yao et al. 2013] in that the zones are best divided along the direction of northeast to southwest. In the northwest zone, winter  $\delta^{18}\text{O}_p$  is low and summer  $\delta^{18}\text{O}_p$  is high. The seasonal variation in  $\delta^{18}\text{O}_p$  is about  $\pm 10$  ‰. The vapor originates from the arid western region of the Tibetan Plateau, the low vapor content in the source region results in low precipitation on the Tibetan Plateau. In the southeast zone of the Tibetan Plateau, the seasonal  $\delta^{18}\text{O}_p$  signal is the opposite of that in the northeast zone.  $\delta^{18}\text{O}_p$  is low in the summer and high in the winter with a difference of  $\pm 15$  ‰. This region is under the influence of the Indian and East Asian monsoon system and receives large amounts of precipitation in summer. In the transition zone (middle zone),  $\delta^{18}\text{O}_p$  is low in the winter and higher in the summer but the difference is smaller with about  $\pm 5$  ‰.

(4) Spatial and temporal variation of  $\delta^{18}\text{O}_p$  and isotopic lapse rates were analyzed.  $\delta^{18}\text{O}_p$  lapse rates of  $\sim -3.1$  ‰/km are present in both the winter and summer season at the Himalayan front of the Tibetan Plateau. At the western side of the Tibetan Plateau a lapse rate of  $\sim -3.4$  ‰/km was observed in the winter, the lapse rate decreases to  $-1.7$  ‰/km in the summer.

(5) Zonal wind patterns and trajectories indicate a seasonal difference of  $\delta^{18}\text{O}_p$  vapor sources. Vapor originates from the western arid region in the winter and

is delivered across most the Tibetan Plateau. The middle and southeast zones of the Tibetan Plateau receive summer vapor from the Indian Ocean. The vapor source influences  $\delta^{18}\text{O}_p$  because air masses with different vapor sources have different starting isotope fractions that have an influence on the isotope composition at a target region [e.g. Bowen and Revenaugh, 2003].

(6) Our analysis for the causes of extreme  $\delta^{18}\text{O}_p$  shows that extreme high  $\delta^{18}\text{O}_p$  values correspond with lower precipitation rates for specific locations.

Furthermore, there is no relationship between temperature and extreme low or high  $\delta^{18}\text{O}_p$  values. Vapor source has been shown to be an important control on the  $\delta^{18}\text{O}_p$  during the Indian monsoon season for the monsoon influenced regions. Vapor from the north and southwest (especially from west of the Arabian Sea) generally coincides with extreme high  $\delta^{18}\text{O}_p$  daily values, while vapor from the Indian Ocean results in mean to extreme low  $\delta^{18}\text{O}_p$  values. Therefore, variations in vapor source are interpreted to be one important cause of the spatial-temporal differences in  $\delta^{18}\text{O}_p$ .

(7) The agreement between the RDM and ECHAM5-wiso simulated  $\delta^{18}\text{O}_p$  at the Himalaya front (86E-94E) during the monsoon season suggests that the simplified RDM approach for estimating lapse rates is appropriate at this location under modern-day conditions. GCM  $\delta^{18}\text{O}_p$  differs from the RDM results at the near surface (~2km), and at >4km elevation with a maximum difference of < 1‰. The changes in  $\delta^{18}\text{O}_p$  due to the exchange of an air parcel with the surrounding environment at the Himalaya front is not significant, the mixing rate is less than 0.2 ‰/h.

## Acknowledgements

This work was supported by a German science foundation grant (DFG-EH329/2-1) to T. Ehlers through the German science foundation (DFG) Priority Program 1372. ('Tibetan Plateau: Formation, Climate, Ecosystems). We thank the DKRZ computing center in Hamburg, Germany for cluster computing time used for this study. The data are available from the authors upon request ([todd.ehlers@uni-tuebingen.de](mailto:todd.ehlers@uni-tuebingen.de)). Two anonymous reviewers are thanked for their constructive reviews of the manuscript.

Author Manuscript



Zone	Location	$\delta^{18}\text{O}_p$ daily Percentile	January			August		
			$\delta^{18}\text{O}_p$ ( $\sigma$ ) ‰	T ( $\sigma$ ) °C	P ( $\sigma$ ) mm/day	$\delta^{18}\text{O}_p$ ( $\sigma$ ) ‰	T ( $\sigma$ ) °C	P ( $\sigma$ ) mm/day
NW	F	>95%	<b>-6.23</b> (1.92)	-24.03 (4.23)	<b>0.57</b> (0.57)	0.68 (0.72)	0.55 (1.54)	0.42 (0.64)
		=Mean	-16.71 (0.29)	-22.51 (4.05)	2.21 (2.00)	-5.30 (0.27)	0.39 (1.29)	2.23 (1.83)
		<05%	<b>-29.90</b> (2.57)	-22.53 (5.03)	<b>2.78</b> (2.10)	-16.08 (1.88)	0.63 (1.28)	3.32 (3.23)
Middle	A	>95%	-2.92 (3.40)	-21.46 (5.49)	0.20 (0.28)	-0.16 (0.60)	2.10 (1.37)	1.41 (2.32)
		=Mean	-11.72 (0.30)	-21.62 (4.90)	1.23 (1.52)	-9.90 (0.30)	1.98 (1.37)	5.91 (5.32)
		<05%	-21.64 (1.93)	-18.44 (4.68)	3.64 (3.43)	-28.2 (1.95)	2.22 (1.12)	16.32 (5.88)
SH	B	>95%	-8.57 (2.37)	-19.88 (2.72)	0.35 (0.26)	-0.64 (2.17)	0.50 (2.0)	0.98 (1.23)
		=Mean	-18.14 (0.28)	-19.80 (2.53)	0.81 (0.63)	-10.00 (0.30)	1.08 (1.86)	3.49 (3.73)
		<05%	-27.33 (1.85)	-21.19 (3.12)	0.65 (0.63)	-23.08 (1.58)	2.27 (1.56)	8.32 (5.27)
SH	C	>95%	1.35 (0.48)	-6.35 (2.68)	0.24 (0.16)	<b>-1.97</b> (0.91)	10.08 (0.84)	<b>6.94</b> (7.30)
		=Mean	-5.88 (0.25)	-6.52 (1.86)	3.02 (3.85)	-11.48 (0.28)	9.72 (0.75)	26.01 (18.35)
		<05%	-18.38 (2.80)	-5.10 (3.46)	7.16 (9.46)	<b>-21.54</b> (1.71)	9.06 (0.70)	<b>54.65</b> (27.06)
SH	D	>95%	0.79 (1.62)	-16.92 (2.03)	0.08 (0.03)	-7.31 (1.14)	2.11 (2.45)	3.82 (3.36)
		=Mean	-10.18 (0.31)	-15.66 (1.52)	1.14 (0.74)	-19.53 (0.28)	3.12 (1.13)	10.84 (7.42)
		<05%	-21.92 (1.41)	-13.81 (3.64)	3.15 (2.79)	-30.88 (1.67)	2.10 (1.00)	19.14 (7.26)
SH	E	>95%	-5.88 (1.03)	-13.48 (2.31)	0.30 (0.22)	-5.98 (1.52)	4.83 (2.06)	0.95 (1.80)
		=Mean	-14.92 (0.28)	-12.13 (2.35)	1.36 (1.44)	-16.42 (0.26)	6.21 (1.90)	2.73 (4.26)
		<05%	-23.9 (1.70)	-13.23 (3.23)	2.50 (3.07)	-26.96 (1.10)	6.19 (1.33)	8.45 (9.87)

Table 1. The average and standard deviation of temperature, precipitation and  $\delta^{18}\text{O}_p$  for days with extreme low  $\delta^{18}\text{O}_p$  value, mean  $\delta^{18}\text{O}_p$  value and extreme  $\delta^{18}\text{O}_p$  value at 6 locations for January and August, analyzed from model daily outputs of 30 simulation years.

Author Manuscript

Figure 1: Topography of the Tibetan Plateau region from: (A) GTOPO30 Topography, and (B): ECHAM5 model Topography at resolution T63. The individual mountain ranges are not clearly represented by the model topography.

Figure 2: Schematic of vapor transport in the ECHAM simulation over topography and the hybrid sigma pressure levels used in the back-trajectory analysis. The precipitation is the integration of water vapor at all the atmospheric levels. It does not calculate the water budget of a target region, but provides a representation of the air masses arriving that region.

Figure 3: Simulated seasonal precipitation (top row), surface temperature (middle row), and surface winds (bottom row) for the Tibetan Plateau during winter (DJF) (left column) and summer (JAS) (middle column), and the seasonal difference (JAS – DJF) for precipitation and temperature (right column). The contour line marks the region where the topography exceeds 1500 m elevation.

Figure 4: Simulated DJF(left column), JAS (middle column) and the seasonal difference (JAS – DJF) (right column) for the precipitation-weighted mean  $\delta^{18}\text{O}_p$  (top row) and its standard deviation ( $\sigma$ ) (bottom row) for the Tibetan Plateau. White lines in panel (A) and (B) represents the analyzed  $\delta^{18}\text{O}_p$  cross-sections shown in Figure 8 and 12 longitude of the north-south cross section P – P' at 87.5°E, latitude of the west-east cross section Q – Q' at 33°N and latitude of the second west-east cross

section R - R' at 30°N. The white dash lines in panel (C) illustrates the separation of the three  $\delta^{18}\text{O}_p$  distribution zones. Numbers in panel (C) represent the observational data locations we compared in Figure 11. The locations represented by number are: 1 (Altay), 2 (Urumqi), 3 (Hetian), 4 (Shiquanhe), 5 (Gaize), 6 (Nyatam), 7 (Lasha) and 8 (Yushu). Black dots with letters in panel (D-F) represent the locations where bar-whisker plots in Figure 5-7 are from and the locations used for trajectory analysis shown in Figure 9, 10 and 13. Those locations are: A (Taro Co: 31.18°N, 84.17°E), B (Qang Co: 35.19°N, 89.15°E), C (Nam Co: 30.44°N, 90.47°E), D (Paiku Co: 28.49°N, 85.65°E) and E (Donggi Cona: 35.25°N, 98.5°E).

Figure 5: January (A) and August (B)  $\delta^{18}\text{O}_p$  distribution at location F in the northwest zone. Maximum, mean +  $1\sigma$ , mean, mean -  $1\sigma$  and minimum of the daily  $\delta^{18}\text{O}_p$  values are shown in the box plots. Seasonal trends show low  $\delta^{18}\text{O}_p$  in winter and high  $\delta^{18}\text{O}_p$  in summer, and the seasonal difference in  $\delta^{18}\text{O}_p$  is ~10‰.

Figure 6: January (left column) and August (right column)  $\delta^{18}\text{O}_p$  distribution at location A (top row) and the location B (bottom row) in the middle zone. Labels are the same as in Fig. 5. A similar seasonal trend in  $\delta^{18}\text{O}_p$  (low in winter and high in summer) is presented as in Fig. 5, but with a smaller seasonal difference of ~0‰ - 5‰.

Figure 7: January (left column) and August (right column)  $\delta^{18}\text{O}_p$  distribution at the location C (A, B), the location D (C, D) and location E (E, F) in the southeast zone.

Labels are the same as in Fig. 5. Opposite  $\delta^{18}\text{O}_p$  seasonal trends are observed in this zone as in Figure 5. High  $\delta^{18}\text{O}_p$  is present in the winter and low  $\delta^{18}\text{O}_p$  present in the summer with the seasonal difference of  $\sim 2\text{‰} - 15\text{‰}$  at different locations.

Figure 8: contour map of  $\delta^{18}\text{O}_p$  (A, D) and west-east (cross section P-P' at  $33^\circ\text{N}$ ) (B, E) and north-south (cross section Q-Q' at  $87.5^\circ\text{N}$ ) (C, F)  $\delta^{18}\text{O}_p$  profiles for January (left column) and August (right column). Red line in contour maps marks the region where the topography exceeds 1500m. Red lines in cross section profiles represent the long-term mean  $\delta^{18}\text{O}_p$  value. Green lines represent  $\pm 1\sigma$  value of long-term  $\delta^{18}\text{O}_p$ . Squares show the monthly mean of  $\delta^{18}\text{O}_p$  for 30 simulation years. Blue lines show the topography cross-section profiles.

Figure 9: Calculated January backwards trajectories at 3 atmosphere levels: middle troposphere level (A, D), boundary level (B, E), and surface level (C, F) at location F (left column) in the northwest zone and location C (right column) in the southeast zone. The trajectories are backwards tracked for 10 days.

Figure 10: Calculated August backwards trajectories at 3 atmosphere levels: middle troposphere level (A, D), boundary level (B, E), and surface level (C, F) at the location F (left column) in the northwest zone and at the location C (right column) in the southeast zone. The trajectories are backwards tracked for 10 days.

Figure 11: Simulated (dash line)  $\delta^{18}\text{O}_p$  and observational (solid line)  $\delta^{18}\text{O}_p$  (Tian et al. 2007) comparison. The error bar of the simulated  $\delta^{18}\text{O}_p$  represents the  $\pm 1\sigma$  value.

Figure 12: Annual mean  $\delta^{18}\text{O}_p$  contour map (A) and three  $\delta^{18}\text{O}_p$  cross section profiles at north-south cross section Q-Q' (B), west-east cross section R-R' (C) and west-east cross section P-P' (C). Labels are the same as in Figure.8. Grey lines show the observational stream water  $\delta^{18}\text{O}$  value published in Hren et al. (2009). Triangles show the precipitation weighted mean annual (abbreviated to mean annual afterwards)  $\delta^{18}\text{O}_p$  for the 30 simulation years. Red lines and green lines in cross section profiles represent the mean and  $\pm 1\sigma$  value of the 30 year mean annual  $\delta^{18}\text{O}_p$ .

Figure 13: Backwards trajectories for the extreme  $\delta^{18}\text{O}_p$  condition at location F (left column) and Location C (right column) during January for the boundary layer (top row) and August for the surface layer (middle row) and boundary layer (bottom row). Orange color shows the trajectories for the days with extreme high  $\delta^{18}\text{O}_p$  values, blue color shows that for the days with mean  $\delta^{18}\text{O}_p$  values and green color represents that for the days with extreme low  $\delta^{18}\text{O}_p$  values.

Figure 14: (A) Comparison of  $\delta^{18}\text{O}_p$  simulated by the GCM (triangle) and RDM (circle) approaches. GCM derived moisture was used for the RDM start up. (B) Estimated  $\delta^{18}\text{O}_p$  mixing for monsoon season (JAS) perpendicular to the Himalaya (86E-94E). The Tibetan Plateau is shaded in gray. The vectors show zonally-averaged meridional and vertical wind.

# Author Manuscript

## References

- Armengaud, A., R. Koster, J. Jouzel and P. Ciais (1998), Deuterium excess in Greenland snow: analysis with simple and complex models, *Journal Geophysical Research* 103, 8947-8953.
- Battisti, D. S., Q. Ding and G. H. Roe (2014), Coherent pan-Asian climatic and isotopic response to orbital forcing of tropical insolation, *Journal of Geophysical Research-atmospheres*, 119, 11997-12020, doi:10.1002/2014JD021960.
- Bert, A. (2005), Lagrangian trajectory analysis for the identification of moist airflows producing intense precipitation events over the Alps, 223 pp, University of Trento.
- Boos, W. R., and Z. Kuang (2010), Dominant control of the South Asian monsoon by orographic insulation versus plateau heating. *Nature*, 463, 218-222.
- Bowen, G. J., and J. Revenaugh (2003), Interpolating the isotopic composition of modern meteoric precipitation, *Water Resources Research*, 39 (10).
- Butzin, M., M. Werner, V. Masson-Delmotte, C. Risi, C. Frankenberg, K. Gribanov, J. Jouzel and V. I. Zakharov (2014), Variations of oxygen-18 in West Siberian precipitation during the last 50 years, *Atmospheric Chemistry and Physics*, 14, 5853-5869, doi: 10.5194/acp-14-5853-2014.
- Chen, B., X. Xu, S. Yang, and W. Zhang (2012), On the origin and destination of atmospheric moisture and air mass over the Tibetan Plateau, *Theoretical and Applied Climatology*, 110, 423-435.
- Cole, J. E., R. D. Rind, R. S. Webb, J. Jouzel and R. Healy (1999), Climatic controls on interannual variability of precipitation  $\delta^{18}\text{O}$ : The simulated influence of temperature, precipitation amount and vapor source region, *Journal of Geophysical Research*, 104, D12, 14223-14235.
- Dansgaard, W., H. B. Clausen, N. Gundestrup, C. U. Hammer, S. F. Johnsen, P. M. Kristinsdottir, and N. Reeh (1982), A new Greenland deep ice core, *Science*, 218, 1273-1277.
- DeCelles, P. G., J. Quade, P. Kapp, M. J. Fan, D. L. Dettman, and L. Ding (2007), High and dry in central Tibet during the Late Oligocene, *Earth and Planetary Science Letters*, 253(3-4), 389-401.
- Dirmeier, P. A., and K. L. Brubaker (1999), Contrasting evaporative moisture sources during the drought of 1988 and the flood of 1993, *Journal of Geophysical Research*



- Research-Atmospheres*, 104(D16), 19383-19397.
- Ehlers, T. A., and C. J. Poulsen (2009), Influence of Andean uplift on climate and paleoaltimetry estimates, *Earth and Planetary Science Letters*, 281(3-4), 238-248.
- Feng, R., C. J. Poulsen, M. Werner, C. P. Chamberlain, H. T. Mix, and A. Mulch (2013), Early Cenozoic evolution of topography, climate, and stable isotopes in precipitation in the north American cordillera, *American Journal of Science*, 313, 613-648, DOI 10.2475/07.3013.01.
- Flohn, H. (1987), Recent investigations on the climatogenetic role of the Qinghai-Xizang Plateau: now and during late Cenozoic, reports on the Northeastern part of Qinghai-Xizang(Tibet) Plateau, *science Press*, 387-416 pp, Beijing.
- Gao, J., S. S. P. Shen, T. Yao, N. Tafolla, C. Risi and Y. He (2015), Reconstruction of precipitation  $\delta^{18}\text{O}$  over the Tibetan Plateau since 1910, *Journal of Geophysical Research-atmospheres*, 120, 4878-4888, doi: 10.1002/2015JD023233.
- Galewsky, J. (2009), Orographic precipitation isotopic ratios in stratified atmospheric flows: Implications for paleoelevation studies, *Geology*, 37 (9) 791-794, doi: 10.1130/G30008A.1.
- Garzione, C. N. (2008), RESEARCH FOCUS Surface uplift of Tibet and Cenozoic global cooling, *Geology*, 36(12), 1003-1004.
- Graham, S. A., C. P. Chamberlain, Y. J. Yue, B. D. Ritts, A. D. Hanson, T. W. Horton, J. R. Waldbauer, M. A. Poage, and X. Feng (2005), Stable isotope records of Cenozoic climate and topography, Tibetan plateau and Tarim basin, *American Journal of Science*, 305(2), 101-118.
- He, Y., C. Risi, J. Gao, V. Masson-Delmotte, T. Yao, C.-T. Lai, Y. Ding, J. Worder, C. Frankenberg, H. Chepfer and G. Cesana (2015), Impact of atmospheric convection on south Tibet summer precipitation isotopologue composition using a combination of in situ measurements, satellite data, and atmospheric general circulation modeling, *Journal of Geophysical Research-Atmospheres*, 120, 3852-3871, doi:10.1002/2014JD022180.
- Hofmann, G., M. Werner, and M. Heimann (1998), Water isotope module of the ECHAM atmospheric general circulation model: A study on timescales from days to several years, *Journal of Geophysical Research-Atmospheres*, 103(D18), 23323-23323.
- Hren, M. T., B. Bookhagen, P. M. Blisniuk, A. L. Booth, and C. P. Chamberlain (2009), delta O-18 and delta D of streamwaters across the Himalaya and Tibetan

- Plateau: Implications for moisture sources and paleoelevation reconstructions, *Earth and Planetary Science Letters*, 288(1-2), 20-32.
- Insel, N., C. J. Poulsen, T. A. Ehlers, and C. Sturm (2012), Response of meteoric  $\delta^{18}\text{O}$  to surface uplift - Implications for Cenozoic Andean Plateau growth, *Earth and Planetary Science Letters*, 317, 262-272.
- Insel, N., Poulsen, C. J., Sturm, C., and Ehlers, T. A (2013), Climate controls on interannual variability of Andean precipitation  $\delta^{18}\text{O}$ , *Journal of Geophysical Research: Atmospheres*, doi:10.1002/jgrd.50619.
- Jeffery, M. L., C. J. Poulsen, and T. A. Ehlers, 2012, Impacts of global cooling, surface uplift and an inland seaway on South American paleoclimate and precipitation  $\delta^{18}\text{O}$ , *Geological Society of America Bulletin*, 124, 335-351.
- Jouzel, J., G. Hoffmann, R. D. Koster and V. Masson, (2000), Water isotopes in precipitation: data/model comparison for present-day and past climates, *Quaternary Science Reviews*, 19, 363-379.
- Kutzbach, J. E., P. J. Guetter, W. F. Ruddiman, and W. L. Prell (1989), Sensitivity of Climate to Late Cenozoic Uplift in Southern Asia and the American West - Numerical Experiments, *Journal of Geophysical Research-Atmospheres*, 94(D15), 18395-18407.
- Kutzbach, J. E., W. L. Prell, and W. F. Ruddiman (1993), Sensitivity of Eurasian Climate to Surface Uplift of the Tibetan Plateau, *Journal of Geology*, 101(2), 177-190.
- Langebroek, P. M., M. Werner, and G. Lohmann (2011), Climate information imprinted in oxygen-isotopic composition of precipitation in Europe, *Earth and Planetary Science Letters*, 311(1-2), 144-154.
- Liu, Z. H., L. D. Tian, T. D. Yao, and W. S. Yu (2010), Characterization of precipitation delta O-18 variation in Nagqu, central Tibetan Plateau and its climatic controls, *Theoretical and Applied Climatology*, 99(1-2), 95-104.
- Ma, D., W. R. Boos, and Z. Kuang, (2014): Effects of orography and surface heat fluxes on the South Asian Summer Monsoon. *Journal of Climate*, 27, 6647-6659.
- Majoube, M. (1971), Fractionnement en oxygen 18 et en deuterium entre l'eau et sa vapeur: *Journal de Chimie et de Physique*, 68(10), 1423-1436.
- Nakicenovic, N., J. Alcamo, G. Davis, Bert de Vries, J. Fenhann, S. Gaffin and K. Gregory, 2000, Special Report on Emissions Scenarios: A special report of

Working group III of the intergovernmental panel on climate change, *Cambridge University Press*, New York, NY (US).

- Mutz, S. G., T. A. Ehlers, J. Li, C. Steger, H. Paeth, M. Werner and C. J. Poulsen, Precipitation  $\delta^{18}\text{O}$  over the Himalaya-Tibet Orogen from ECHAM5-wiso Simulations: Statistical Analysis of Temperature, Topography, and Precipitation, *Journal of Geophysical Research-atmospheres*, in press, (<http://onlinelibrary.wiley.com/doi/10.1002/2016JD024856/full>).
- Poulsen, C. J., D. Pollard, and T. S. White, (2007). General circulation model simulation of the  $\delta^{18}\text{O}$  content of continental precipitation in the middle Cretaceous: a model-proxy comparison, *Geology* 35, 199-202.
- Poulsen, C.J., T. A. Ehlers, and N. Insel (2010) Onset of convective rainfall during gradual Late Miocene rise of the Central Andes, *Science*, 328, 490-493.
- Roe, G. H., Q. Ding, D. S. Battisti, P. Molnar, M. L. Clark, and G. N. Garziona (2010), A modeling study of the response of Asian summertime climate to the largest geologic forcings of the past 50 Ma, *Journal of Geophysical Research-atmospheres*, 121, doi:10.1002/2015JD024370.
- Rockner, E., G. Bäuml, L. Bonaventura, R. Brokoph, M. Esch, M. Giorgetta, S. Hagemann, I. Kirchner, L. Kornblueh, E. Manzini, A. Rhodin, U. Schlese, U. Schulzweida, and A. Tompkins (2003), The atmospheric general circulation model ECHAM5. Part I: Model description. Rep. 349Rep., 127 pp, Max Planck Institute for Meteorology, Hamburg.
- Rowley, D. B., and B. S. Currie (2006), Palaeo-altimetry of the late Eocene to Miocene Lunpola basin, central Tibet, *Nature*, 439(7077), 677-681.
- Rowley, D. B., and C. N. Garziona (2007), Stable isotope-based paleoaltimetry, *Annual Review of Earth and Planetary Sciences*, V. 35, 463-508.
- Ruddiman, W. F. and J. E. Kutzbach (1989), Forcing of Late Cenozoic Northern Hemisphere Climate by Plateau Uplift in Southern Asia and the American West, *Journal of Geophysical Research*, 94 (D15), 18,409-18,427.
- Sherwood, S. C., R. Roca, T. M. Weckwerth and N. G. Andronova (2010), Tropospheric water vapor, convection and climate, *Review of Geophysics*, 48 (2), RG2001, doi:10.1029/2009RG000301.
- Starr, K., G. Hoffmann, B. Langmann and W. Stichler (2005), Simulation of  $\text{d}^{18}\text{O}$  in precipitation by the regional circulation model REMOiso, *Hydrological Processes*, 19(17), 3425-3444, doi:10.1002/hyp.5979.

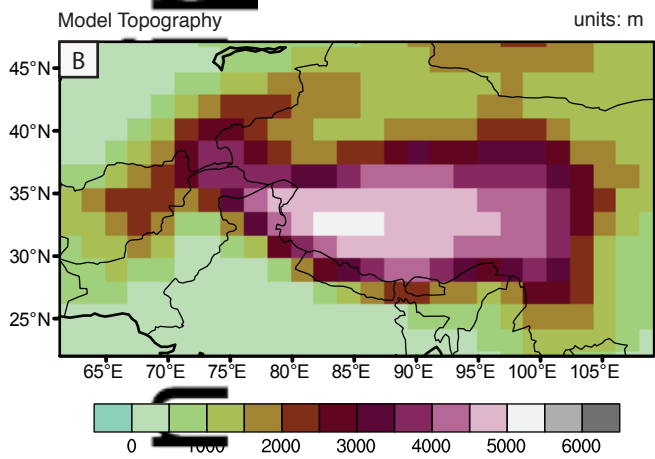
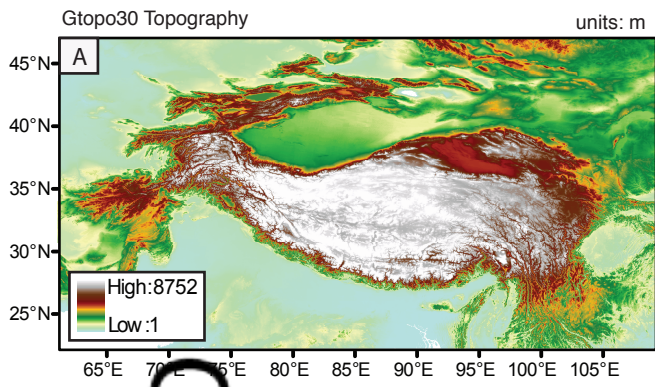
- Sturm, C., F. Vimeux, and G. Krinner (2007), Intraseasonal variability in South America recorded in stable water isotopes, *Journal of Geophysical Research-Atmospheres*, 112(D20).
- Takeshi, K. and D. S. Battisti (2006), Processes controlling the mean tropical precipitation Pattern. Part I: The Andes and the Eastern Pacific ITCZ, *Journal of climate*, 20, 3434-3451.
- Tian, L., T. Yao, Z. Yang, and J. Pu (1997), A 4-year's observation of delta O-18 in precipitation on the Tibetan Plateau, *Journal of Glaciology and Geocryology*, 10(22-36).
- Tian, L. D., T. D. Yao, A. Numaguti, and W. Z. Sun (2001), Stable isotope variations in monsoon precipitation on the Tibetan Plateau, *Journal of the Meteorological Society of Japan*, 79(5), 959-966.
- Tian, L. D., T. D. Yao, K. MacClune, J. W. C. White, A. Schilla, B. Vaughn, R. Wehner, and K. Ichiyanagi (2007), Stable isotopic variations in west China: A consideration of moisture sources, *Journal of Geophysical Research-Atmospheres*, 112(D10).
- Vulle, M., and M. Werner (2005a), Stable isotopes in precipitation recording South American summer monsoon and ENSO variability: observations and model results, *Climate Dynamics*, 25(4), 401-413.
- Vulle, M., M. Werner, R. S. Bradley, and F. Keimig (2005b), Stable isotopes in precipitation in the Asian monsoon region, *Journal of Geophysical Research-Atmospheres*, 110(D23).
- Werner, M., M. Heimann and G. Hoffmann (1998), Stable water isotopes in Greenland ice cores: ECHAM 4 model simulations versus field measurements. In: IAEA, (Ed.) International Symposium on Isotopes Techniques in the study of Past and Current Environmental changes in the Hydrosphere and the Atmosphere. Vienna. 603-612.
- Werner, M., P. M. Langebroek, T. Carlsen, M. Herold, and G. Lohmann (2011), Stable water isotopes in the ECHAM5 general circulation model: Toward high-resolution isotope modeling on a global scale, *Journal of Geophysical Research-Atmospheres*, 116.
- Webster, P. J., V. O. Magana, T. N. Palmer, J. Shukla, R. A. Tomas, M. Yanai and T. Yasunari (1998), Monsoons: Processes, predictability, and the prospects for prediction, *Journal of Geophysical Research*, 103 (C7), 14,451 -14,510.

Yao, T. D., V. Masson, J. Jouzel, M. Stievenard, W. Z. Sun, and K. Q. Jiao (1999), Relationships between delta O-18 in precipitation and surface air temperature in the Urumqi River Basin, east Tianshan Mountains, China, *Geophysical Research Letters*, 26(23), 3473-3476.

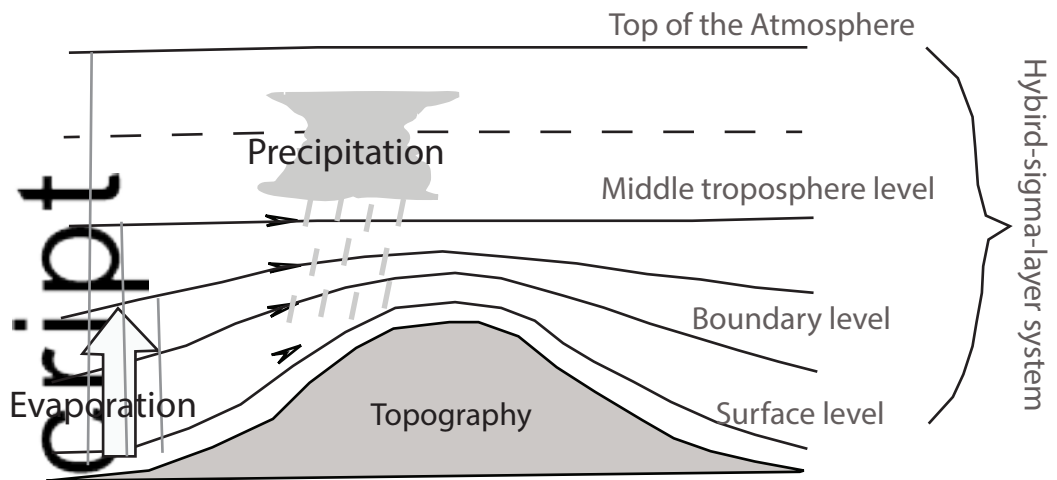
Yao, T., V. Masson-Delmotte, J. Gao, W. Yu, X. Yang, C. Risi, C. Sturm, M. Werner, H. Zhao, Y. He, W. Ren, L. Tian, C. Shi, and S. Hou (2013), A review of climatic controls on in delta O-18 precipitation over the Tibetan Plateau: observations and simulations, *Reviews of Geophysics*, 51(4), 525-548, Doi:10.1002/rog.20023.

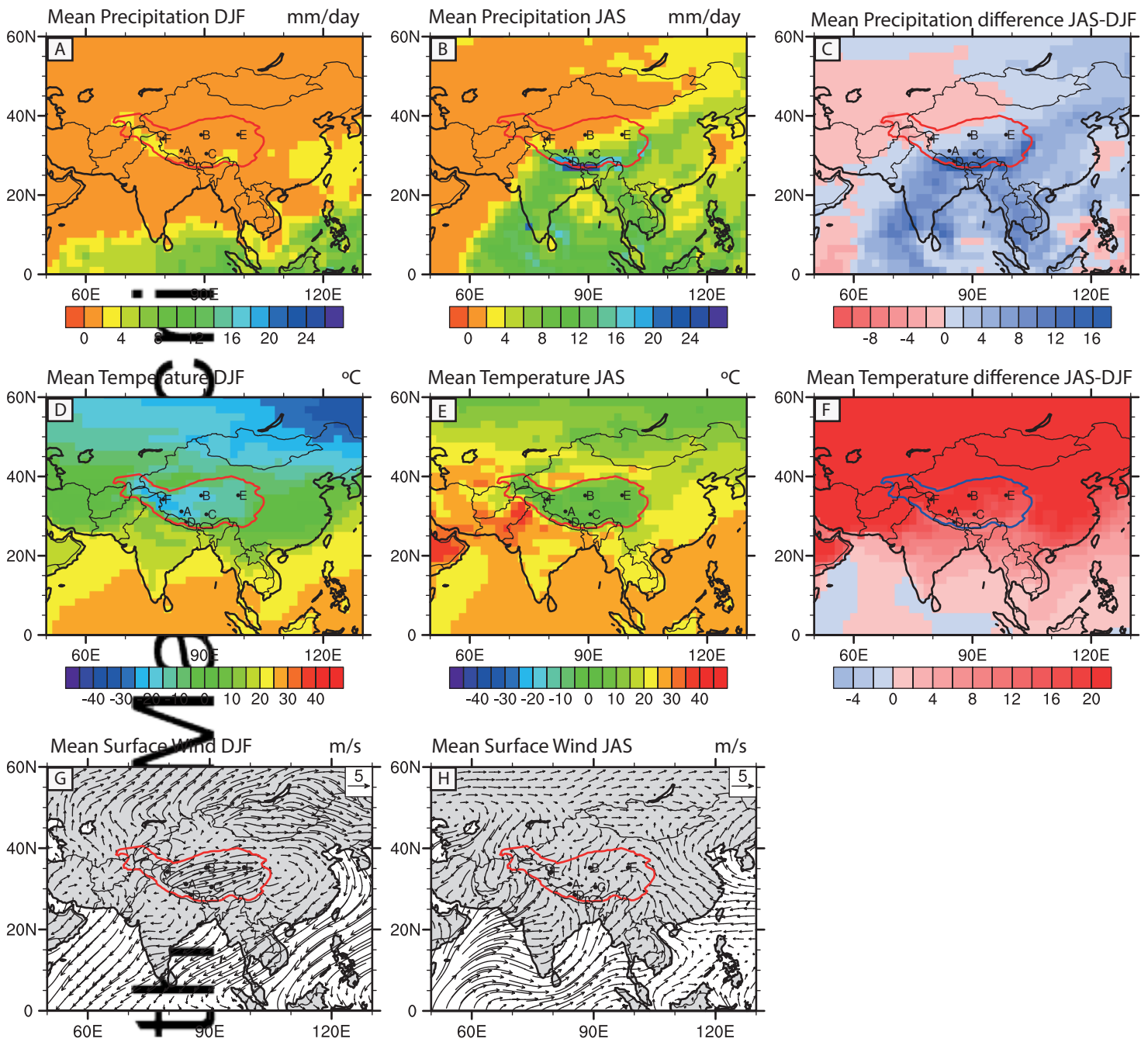
Yurtsever, Y., and J. Gat (1981), Stable isotope hydrology: Deuterium and Oxygen-18 in the water cycle, *Atmospheric waters*, eds. Gat, J. R. and Gonfianini, R., IAEA, Vienna, Austria.

Author Manuscript

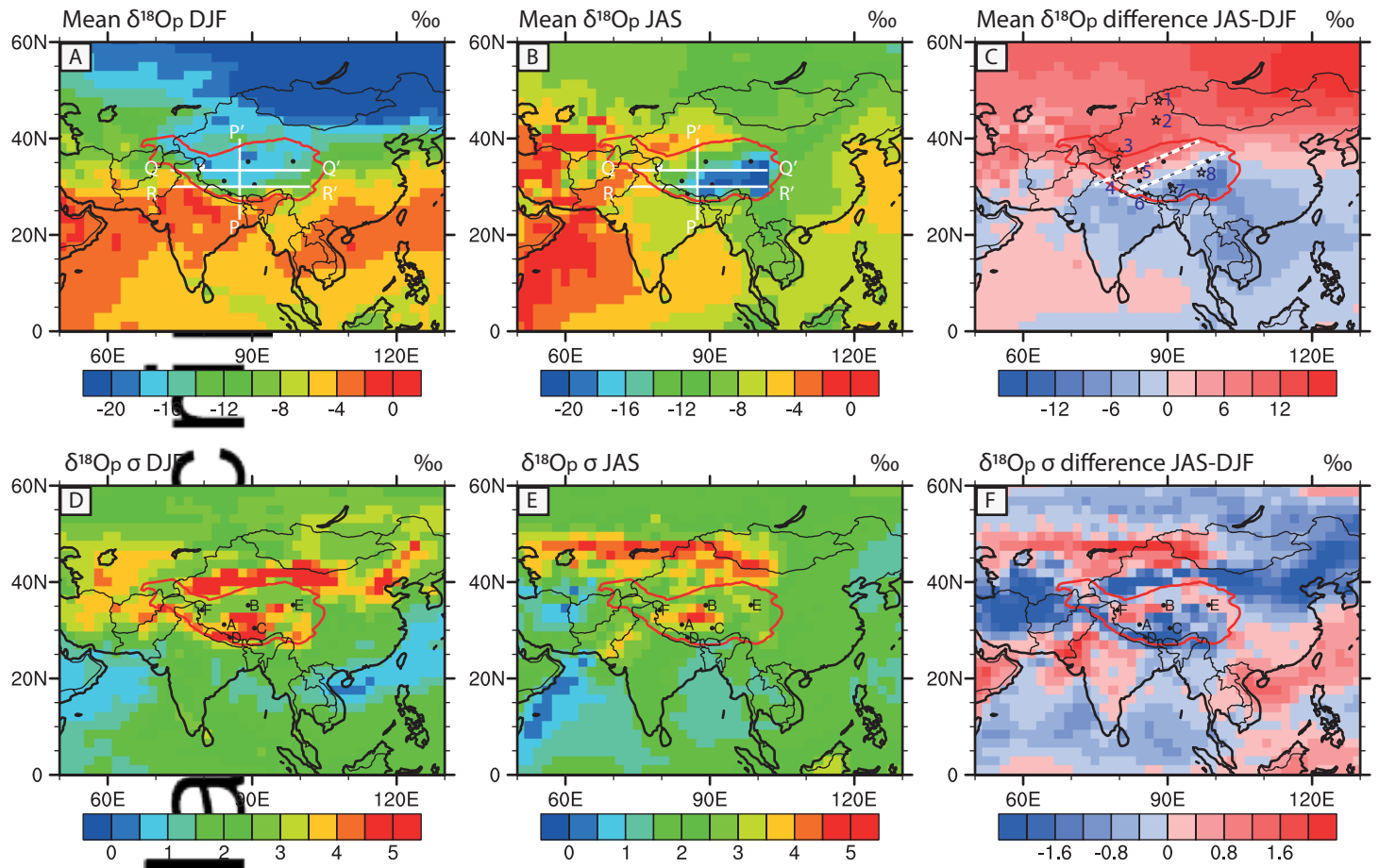


Author Manuscript

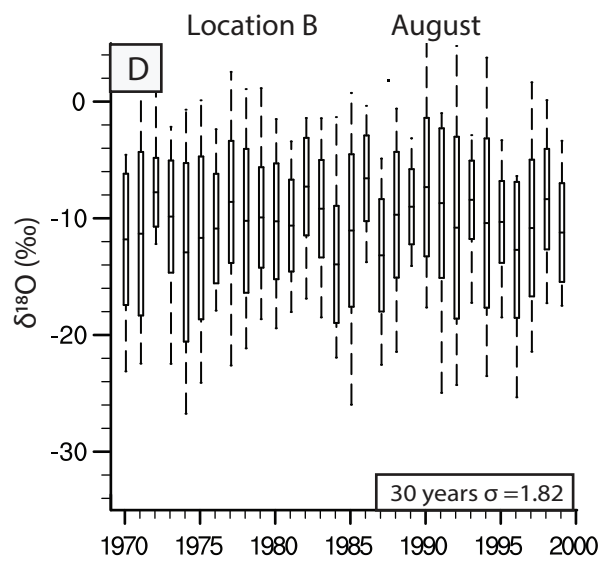
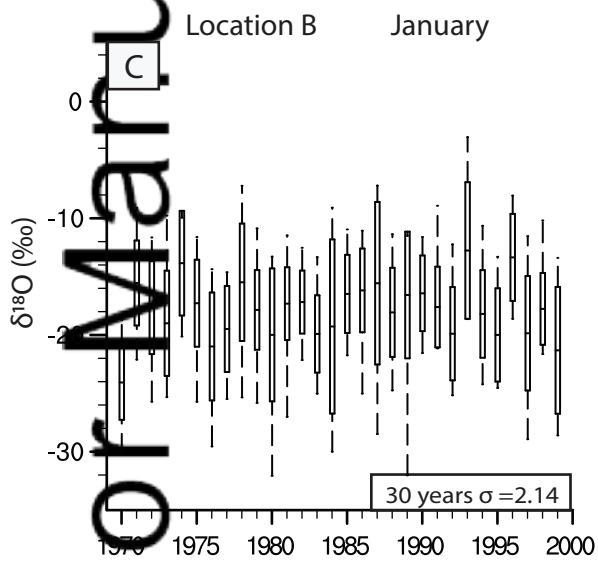
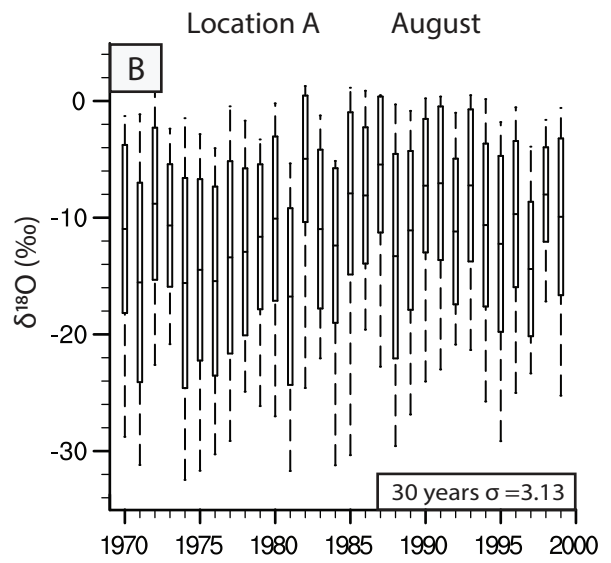
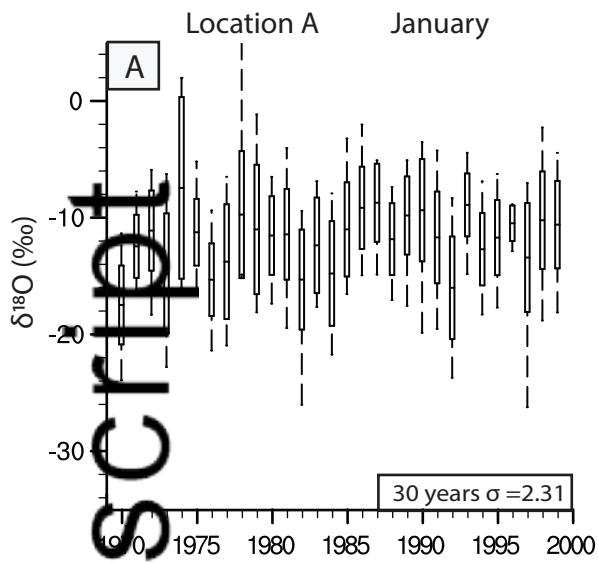


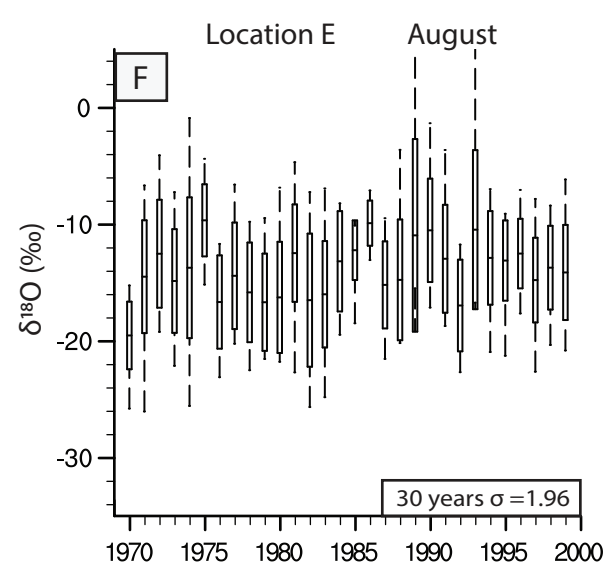
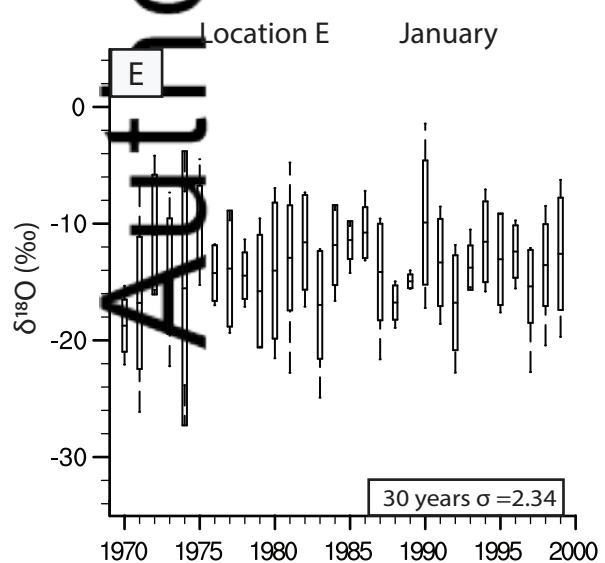
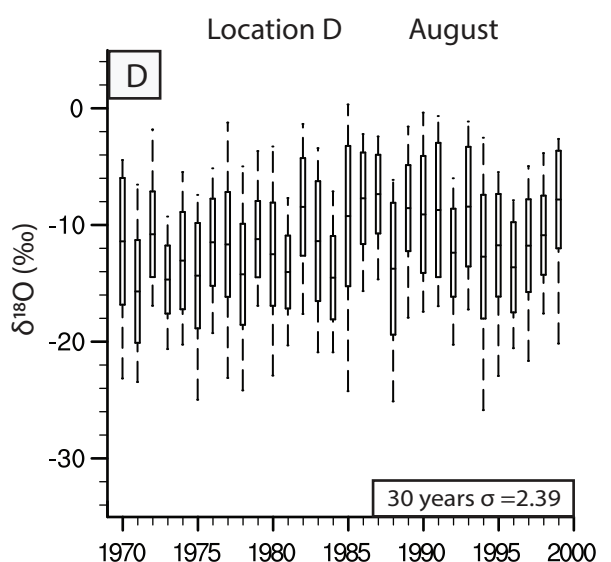
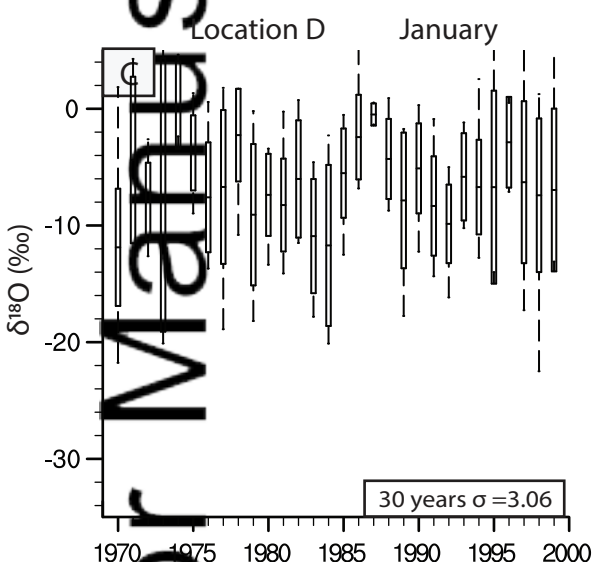
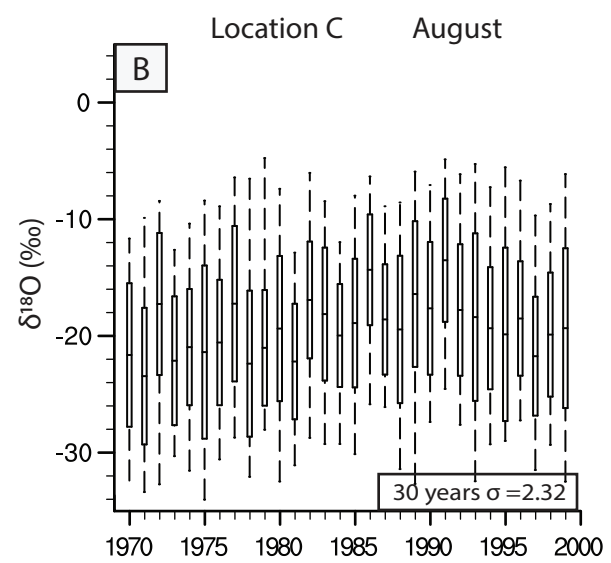
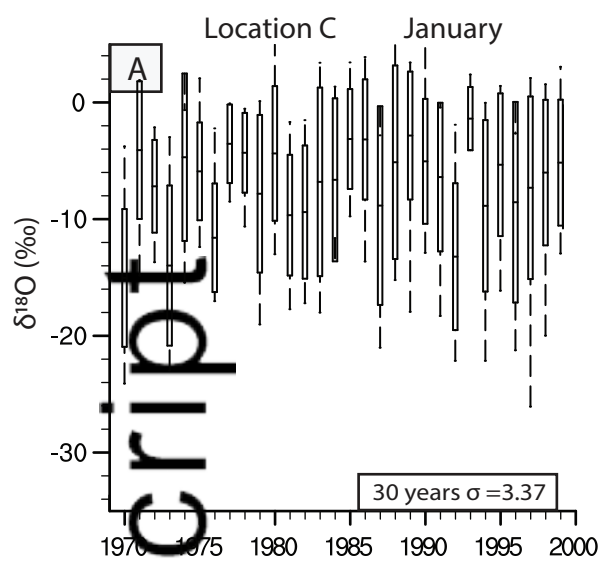


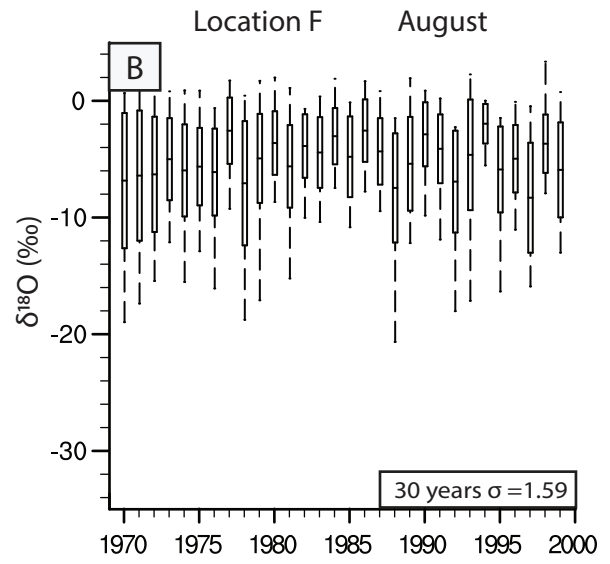
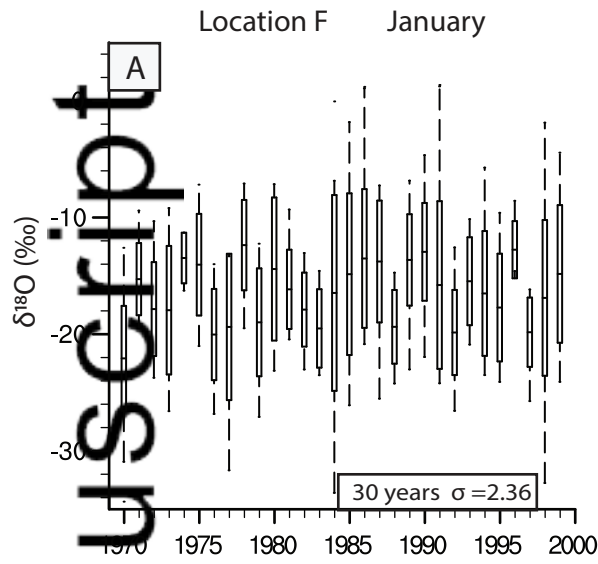


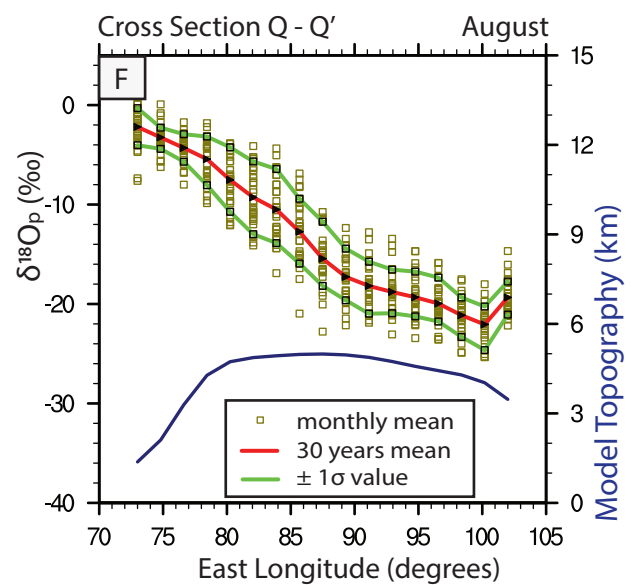
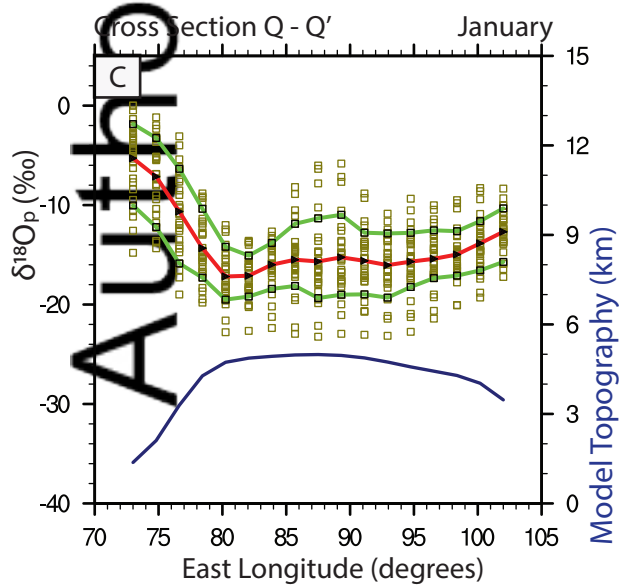
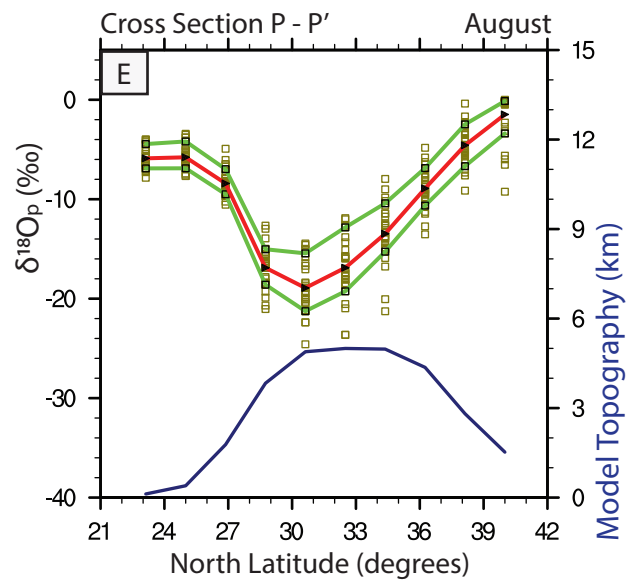
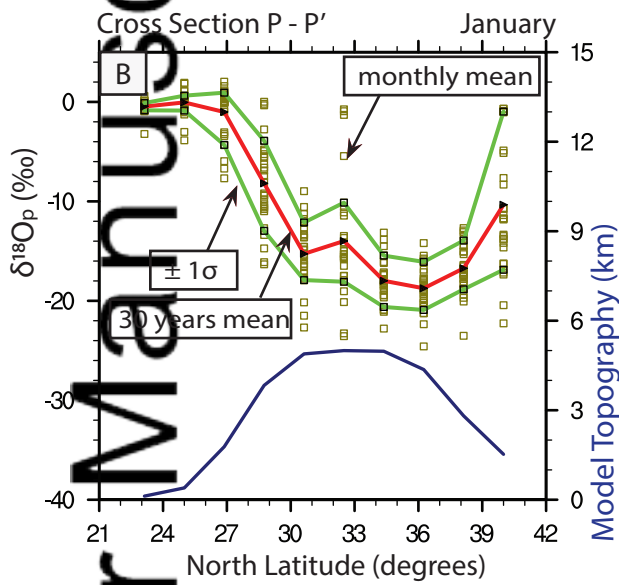
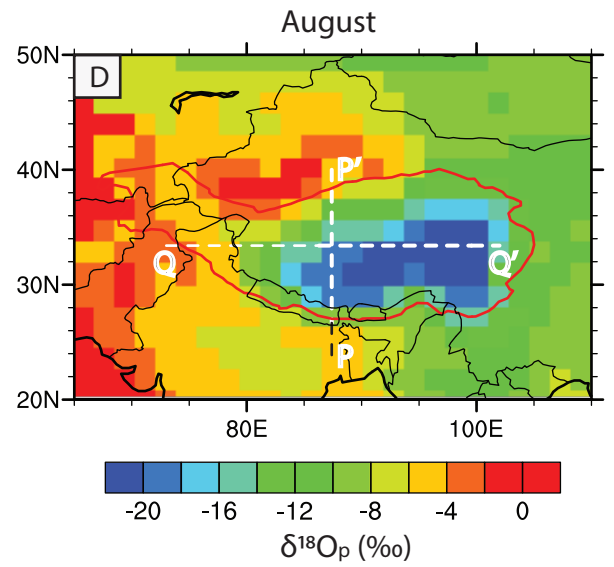
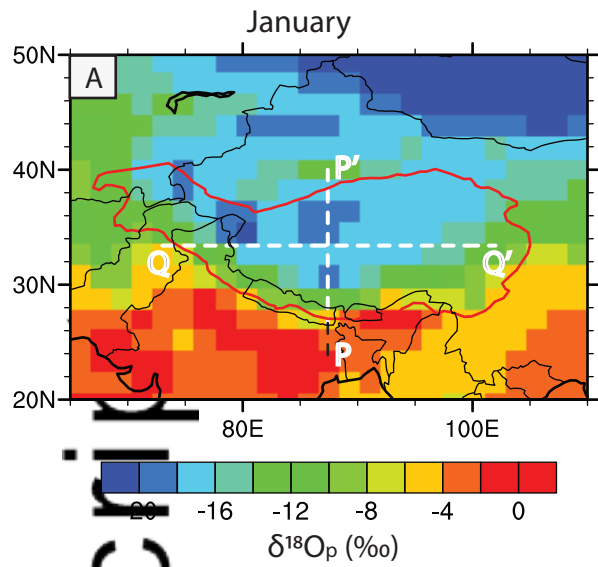


Author Manuscript

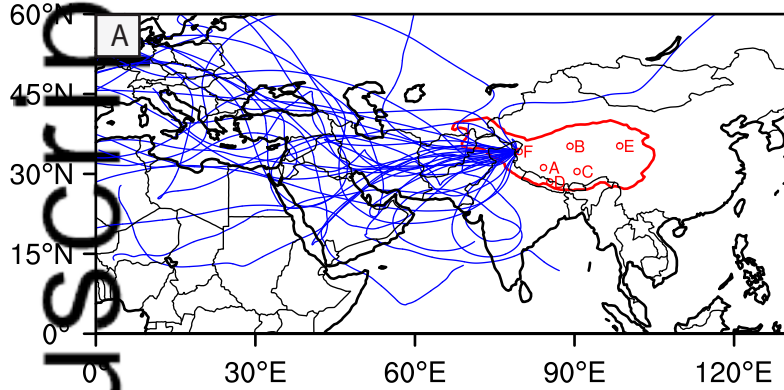




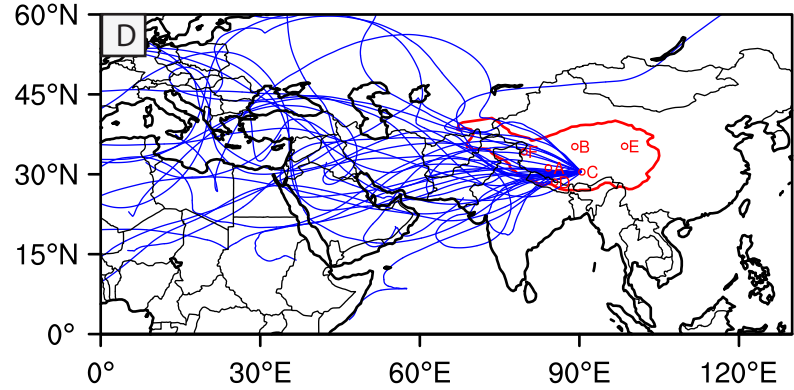




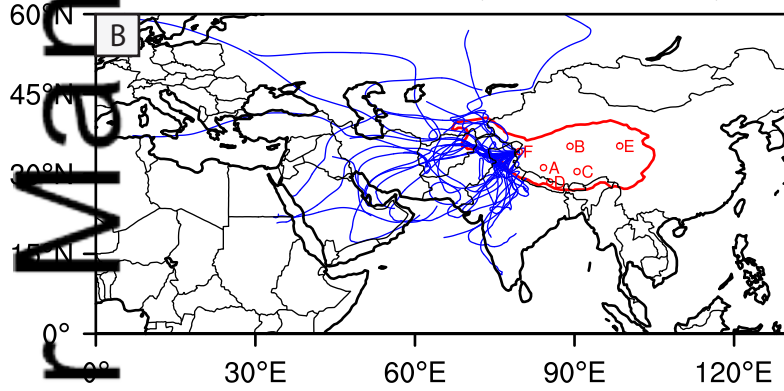
Location F middle troposphere level January



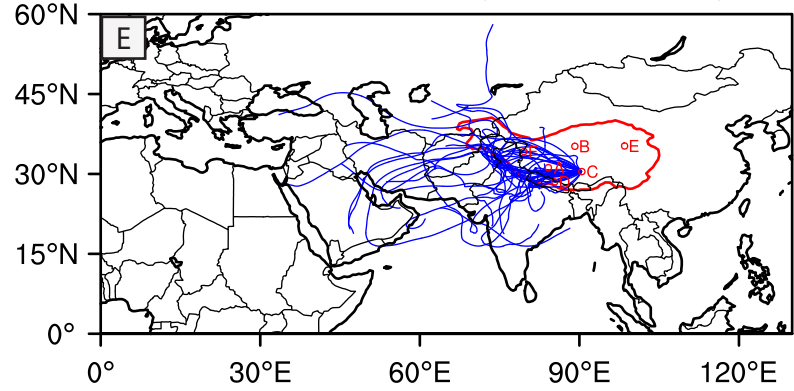
Location C middle troposphere level January



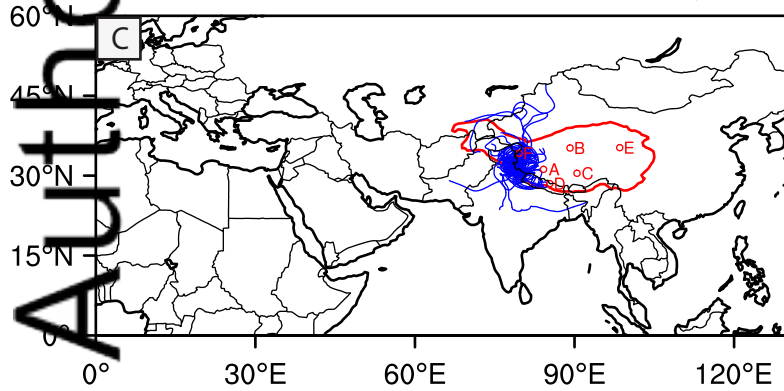
Location F boundary level January



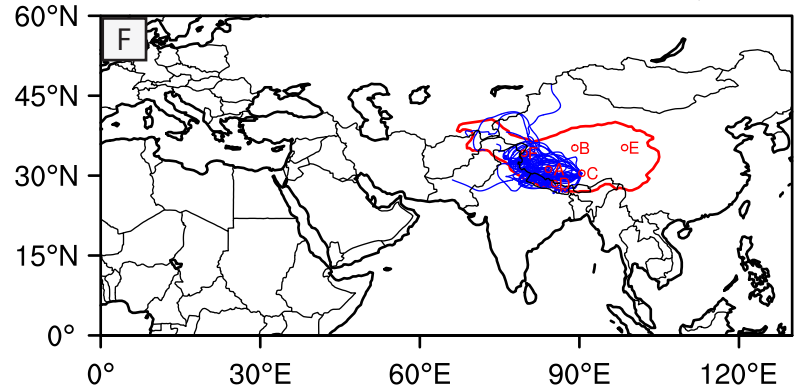
Location C boundary level January



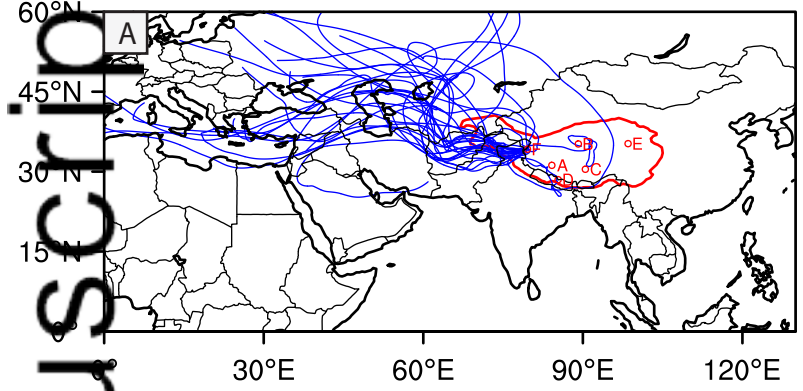
Location F surface level January



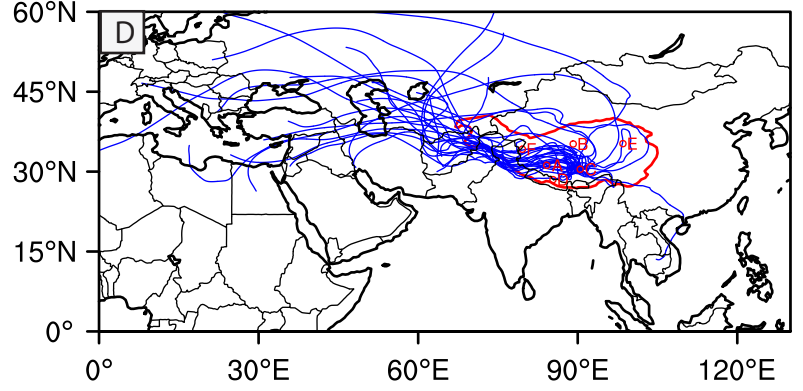
Location C surface level January



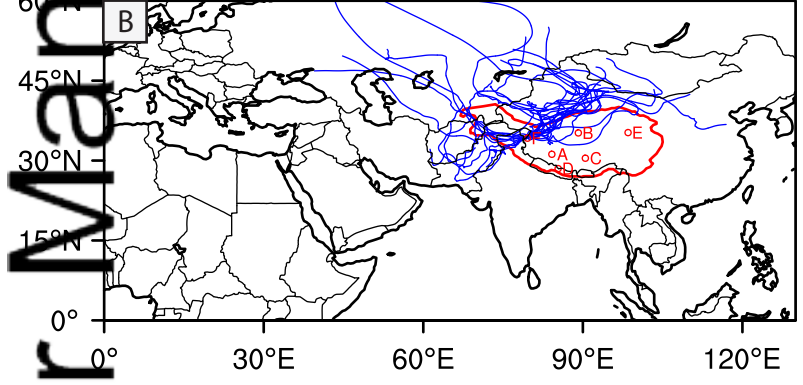
Location F middle troposphere level August



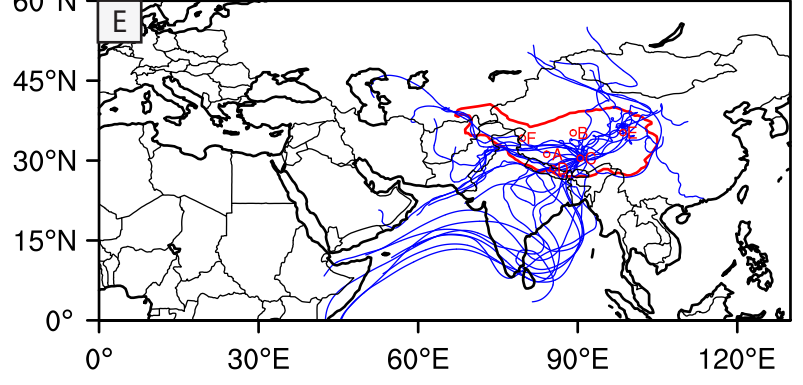
Location C middle troposphere level August



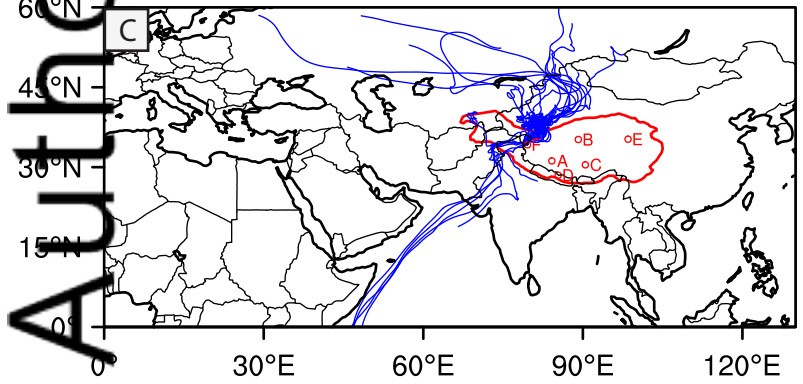
Location F boundary level August



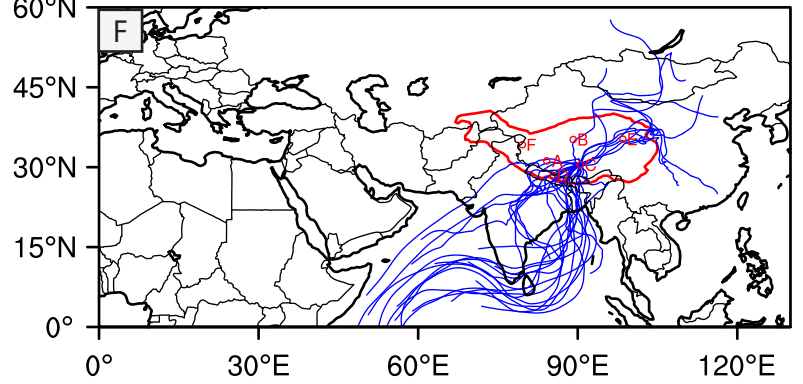
Location C boundary level August



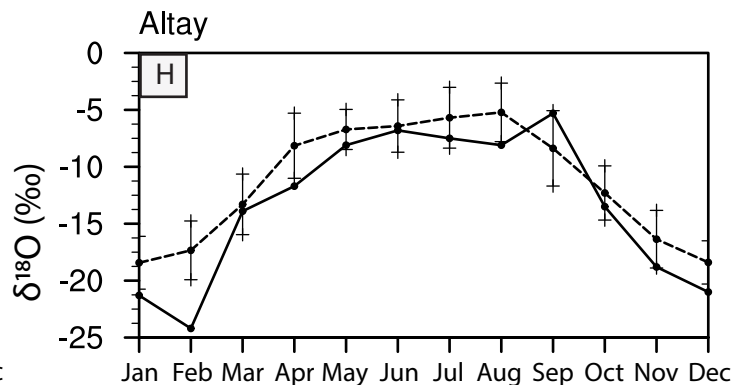
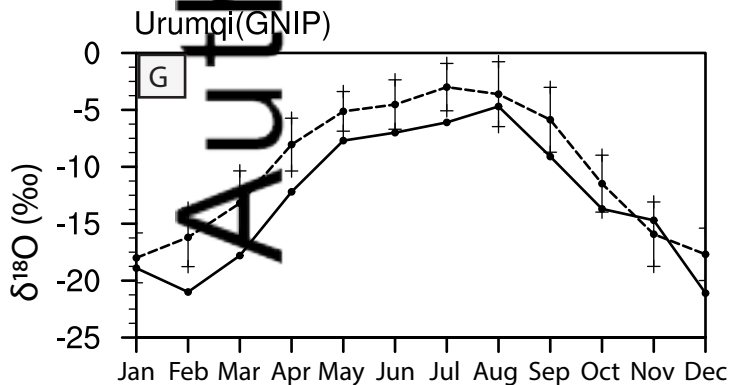
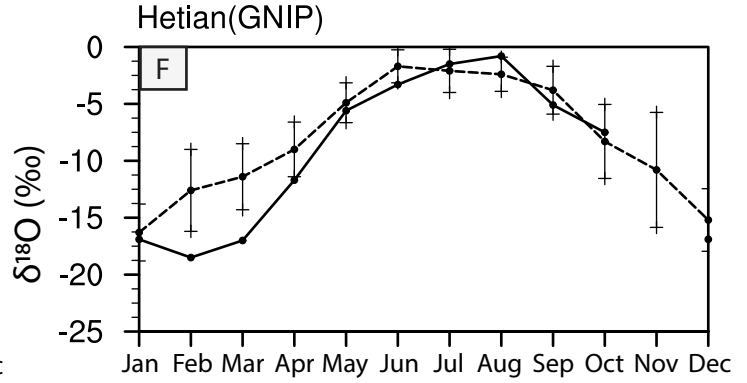
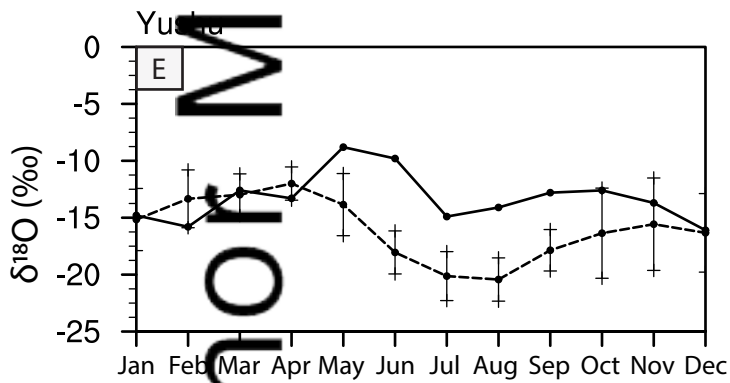
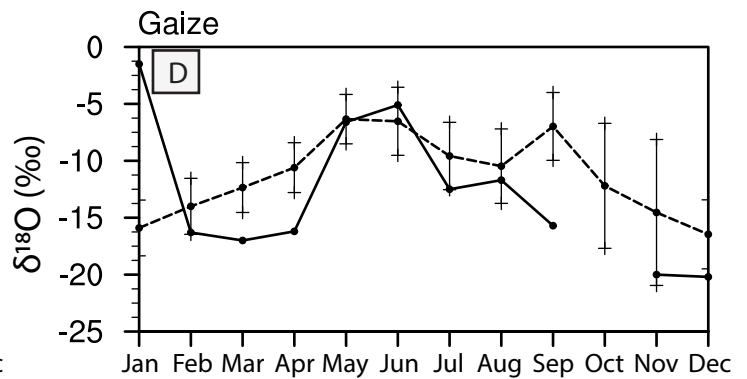
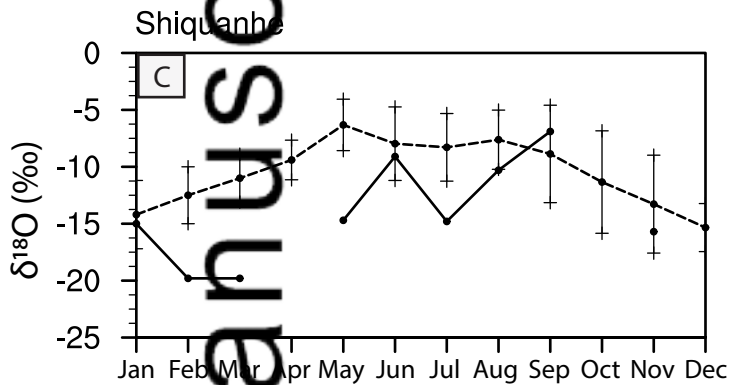
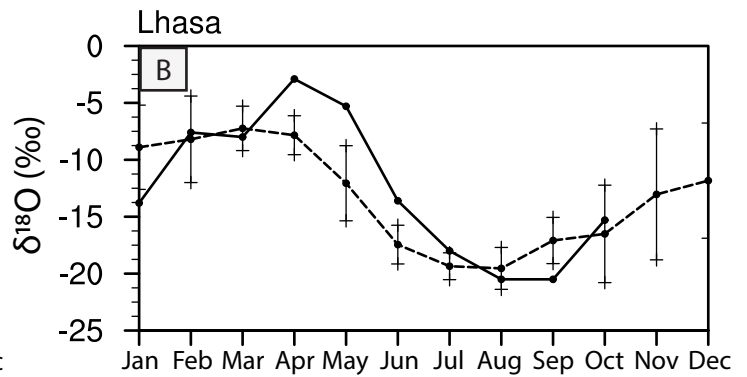
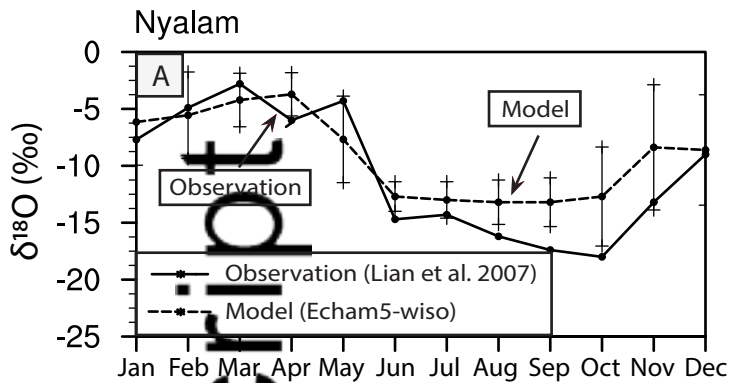
Location F surface level August



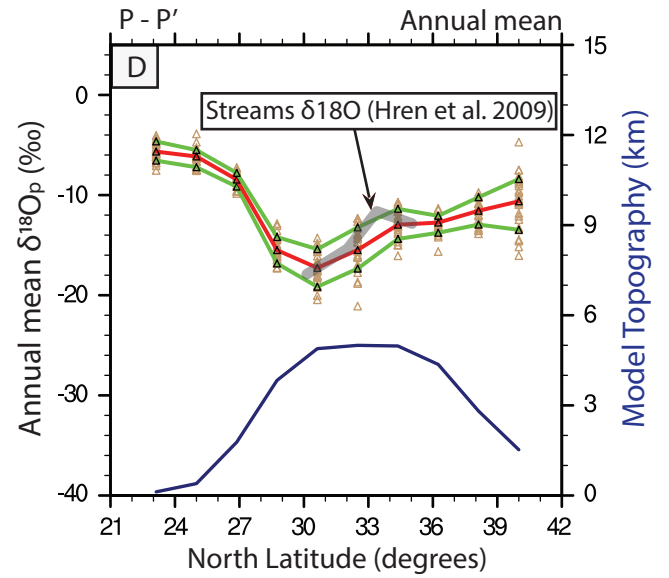
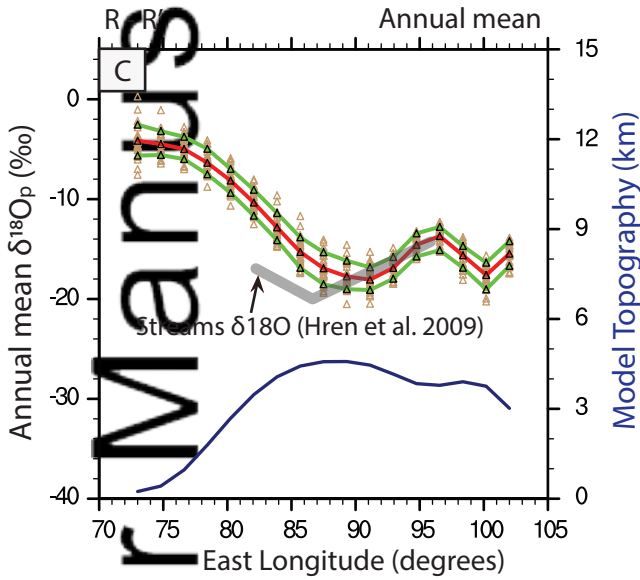
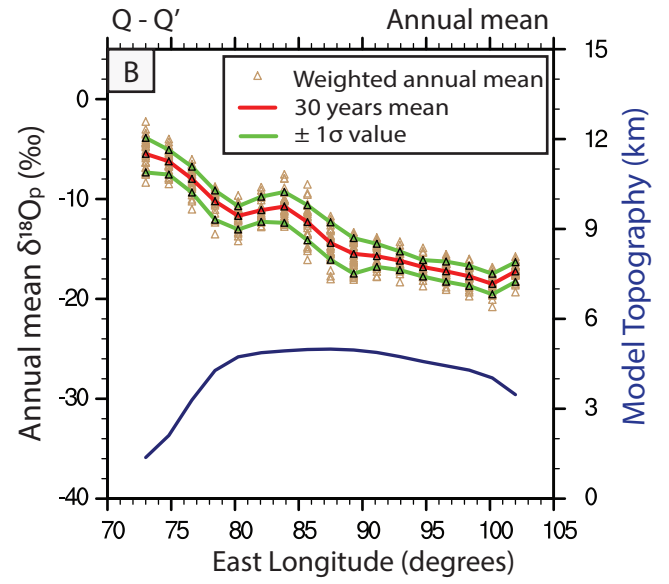
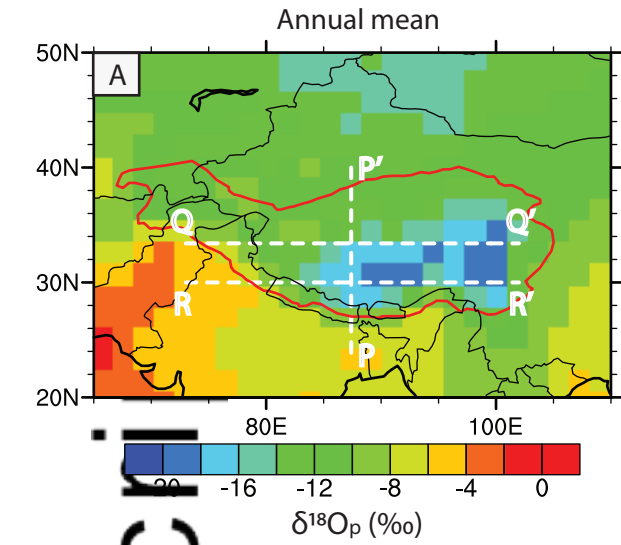
Location C surface level August



Author Manuscript







Author Manuscript

